to be resistant to biological degradation in both extracellular and cytoplasmic environments. Silicone derivatives are known to be very attractive materials, because they exhibit low toxicity and unique physical properties. Therefore they have been widely used as versatile products such as foam stabilizer, rubber, paint, fiber, glass, and textile.[13] In spite of the usage of polysiloxane in wide fields, polysiloxane has not been studied so far in terms of polymeric materials for nanoparticles that are aimed at drug delivery system. Although biodegradable polymers have been extensively studied as polymeric materials for nanocarriers, a recent review article indicates the toxicological problems associated with degradation products of biodegradable polymeric carriers.[14] Polysiloxane has noteworthy properties with regard to degradation, stability and durability, based on a self-repair mechanism where silanol groups generated by the degradation of siloxane backbone can condense each other to form new siloxane bonds.[12] Polysiloxane with stability and inertness is expected to achieve reduced toxicity and longer circulation in terms of their usage as a drug carrier. Here, we describe nanoparticle formation of amphiphilic polysiloxane, cellular uptake of polysiloxane nanoparticles via caveolae of membrane microdomains, and influence of polysiloxane nanoparticles on cellular function; nitric oxide release in human aortic endothelial cells.

Experimental Section

Materials. Amphiphilic polysiloxane (Am-PAPS) was prepared by the method described in our previous report.[15] Am-PAPS was labeled with fluorescein thioisocyanate and was named Flu-Am-PAPS. Rabbit anti-caveolin-1 IgG was purchased from Sigma (St. Louis, MI). Mouse anti-eNOS IgG and mouse antiphospho-Ser1177-eNOS IgG was purchased from BD Transduction Laboratories (Franklin Lakes, NJ). Rabbit anti-fluorescein IgG was purchased from Molecular Probes (Eugene, OR). Anti-rabbit IgG conjugated with gold nanoparticles (5 nm in diameter) was purchased from GE healthcare. TRITC-labeled anti-rabbit IgG and TRITC-labeled anti-mouse IgG were purchased from Molecular Probes (Eugene, OR). HRP conjugated antimouse IgG was purchased from Cell Signaling Technology (Danvers, Mass). Monosulfo-*N*-hydroxy-succinimido nanogold (NANOGOLD) was purchased from Nanoprobes (Yaphank, NY). Gold nanoparticle labeled Am-PAPS (Au-Am-PAPS) was prepared by coupling NANOGOLD to the amphiphilic polysiloxane. All other reagents were purchased from Gibco, Nacalai Tesque, Sigma, or Wako Pure Chemicals unless otherwise indicated.

Nanoparticles Suspension. Aqueous suspension of each amphiphilic polysiloxane (Am-PAPS, Flu-Am-PAPS, or Au-Am-PAPS) was prepared by dispersing it (initial concentration: 1 mg/mL) into cell culture medium (EGM-2; Cambrex) and sonication with bath-type ultrasound washer (25 W and 40 kHz for 5 min). The suspension was passed through the membrane filters with the pore size of 0.45 μm (Millex-GV; Millipore) and 0.22 μm (Millex-GV; Millipore) for sterilization. Concentration of Flu-Am-PAPS was determined by fluorescence spectroscopy and was 0.1 mg/mL that was based on calibration with fluorescein-labeled sugar conjugated PAPS (1 mg/mL dissolved in EGM-2).

Measurements. The ^{1}H NMR spectra (600 MHz) were recorded using a JEOL ECA600 spectrometer. Fluorescence spectra for quantitative analysis were obtained on a fluorescence spectrometer (RF-5300 PC: Shimadzu) using a quartz cuvette (1 mm path length). The dynamic light scattering (DLS) measurement was performed on a Zetasizer 3000 (Malvern Instruments). Morphological study of nanoparticles was carried out by scanning electron microscope (Hitachi S-4100 electron microscope). The observation of plasma membrane and cytosol of human aortic endothelial cells was performed by a transmission electron microscope (Tecnai G2 *Sphera*, FEI, U.S.A.). Fluorescence imaging was performed on a IX-71 (Olympus) equipped with a fluorescence mirror unit, U-MNIBA3 (band-pass filter from 470 to 495 nm for excitation light and using a long pass filter from 510 to 550 nm for emission light) for the detection of fluorescein emission and U-MWIG3 (band-pass filter from 530 to 550 nm for excitation light and using a long pass filter >575 nm for emission light) for the detection of rhodamine emission. High-pressure mercury lamp (USH-1030 L: Olympus) was used as a light source for the fluorescence microscopy and was powered by a power supply (BH2-RFL-T3: Olympus).

Cell Culture Experiment. Human aortic endothelial cells (HAECs) were purchased as cryopreserved samples of third passage (Lot: 4F1350) from Cambrex, Wakersville, MD. The HAECs used in the experiment were fourth passage. Polystyrene dishes (ϕ35 mm, Iwaki) were filled with 2 mL of a supplemented culture medium (EGM-2; Cambrex) and equilibrated in a 37 °C, 5% CO_2 humidified incubator for 30 min before cell seeding. After the frozen cells were thawed at 37 °C, 70 μL of the cell suspension (8.0×10^5 cells/mL, viability: 85% (determined by trypan blue exclusion test)) were seeded in the culture dishes. The cell-seeded plates were placed in a 37 °C, 5% CO_2 humidified incubator. The HAECs were cultured for 72 h before the medium exchange with nanoparticle suspension. For fluorescence microscopy observation, the cells were rinsed with PBS (warmed at 37 °C), fixed by immersing into 10% formaldehyde neutral buffer solution (Nacalai tesque) at room temperature (22 °C) for 15 min and washed three times with PBS (Gibco). Fluorescence images used for the quantitative analysis of the cellular uptake of nanoparticles were taken at the constant exposure time to compare fluorescence intensity of the images at prescribed incubation time. Fluorescence images of the cells were taken by a fluorescence microscope (IX71; Olympus) equipped with a CCD camera (DP70; Olympus). To perform quantitative evaluation of fluorescence intensity, the fluorescence images were taken at the same exposure time (1/6.0 s). The exposure time was automatically measured by the operating software of DP70. The appropriate exposure time was chosen under the condition that over exposed images should be avoided to calculate fluorescence intensity of the images as correct as possible. The excess over exposure and under exposure could be prevented when the exposure time was set at 1/6.0 s that was measured when the HAECs exposed to Flu-Am-PAPS for 6 h were photographed by DP70. Fluorescence intensity of the incorporated nanoparticles of Flu-Am-PAPS was measured by integrating the fluorescence intensity observed at each pixel of the fluorescence images using image analysis software (Fluoview ver. 5.0; Olympus).

Cytotoxicity Assay. Cytotoxicity of polysiloxane nanoparticles were assessed using Cell Count Reagent SF (Nacalai Tesque, Kyoto) as a colorimetric indicator for living cells. HAECs were seeded in each well of 96-well plates and were incubated in a 37 °C, 5% CO_2 humidified incubator for 24 h before cytotoxicity assay. Cell number in each well was adjusted by stepwise 2-fold dilution of HAECs cell suspension. The cell number per well ranged from 5000 to 40000 cells. The total amount of the cell suspension including growth medium was 100 μL per well. The growth medium was replaced with 100 μL of a suspension of polysiloxane nanoparticle (1 mg/mL) for cytotoxicity testing. After 6 or 24 h incubation, each well was rinsed with 100 μL of growth medium to remove polysiloxane nanoparticles and was filled with 100 μL of fresh growth medium. Then, 10 μL of Cell Count Reagent SF solution containing WST-8 (5 mM),[16] colorimetric indicator, was added to each well to evaluate cell viability. HAECs were incubated with WST-8 for 4 h. WST-8 is converted to water-soluble formazan by an electron mediator coupled to the intracellular reduction of NAD^+. Absorbance of each well was measured at 450 nm using a microplate reader (Model 680, Bio-Rad, Hercules, CA). Cell viability was evaluated by the following equation: (cell viability) = (Abs for samples to be tested − Abs for blank)/(Abs for control − Abs for blank) × 100, "Abs" stands for absorbance of each well at 450 nm.

Immunostaining. To visualize the localization of caveolin-1 and endothelial nitric oxide synthase (eNOS) in HAECs, each antigen was stained by immunological method using primary antibodies (rabbit anti-caveolin-1 IgG; Sigma and mouse anti-eNOS IgG; BD) and fluores-

cence labeled secondary antibodies (TRITC labeled anti-rabbit IgG and TRITC labeled anti-mouse IgG; Molecular Probes). For immunostaining, cells were fixed by 10% formaldehyde neutral buffer solution (Nacalai tesque) at room temperature (22 °C) for 15 min and permeated with 0.1% PBS (pH 7.2, Gibco) solution of Triton X-100 (Sigma) for 5 min at 20 °C. After 1 h of blocking with 1% normal goat serum solution, HAECs were incubated with a primary antibody (200 times dilution with 0.1% normal goat serum solution) for 1 h. The HAECs treated with primary antibody were incubated with fluorescent dye labeled secondary IgG for 1 h. Fluorescence images of the cells were taken by a fluorescence microscope (IX71; Olympus) equipped with a CCD camera (DP70; Olympus) and confocal laser scanning microscope (FV 100; Olympus).

Transmission Electron Microscopy (TEM). Two types of specimens, ultrathin section and rapid-freeze, deep-etch, freeze-replica, were prepared for the observation of fine structure of plasma membrane and cytosol in cells using transmission electron microscopy. HAECs were grown on carbon-coated sapphire glass with a diameter of 5 mm for 2 days after inoculation. Specimens for ultrathin section were prepared by the following method. For the TEM observation of polysiloxane nanoparticles in caveolae, HAECs were exposed to gold nanoparticle labeled Am-PAPS (Au-Am-PAPS) dispersed in growth medium (EGM-2) for 3 h. After a 3 h incubation with Au-Am-PAPS, the HAECs attached on coverslips were washed with NaHCa buffer (30 mM HEPES, 100 mM NaCl, 2 mM $CaCl_2$, pH 7.3) and treated with chemical fixation reagent (2.5% glutaraldehyde (GA), 150 mM sucrose in PBS buffer). In the case of the immunodetection of caveolae in HAECs, HAECs were fixed with NaHCa buffer containing 4% paraformaldehyde for 1 h, then treated with a quenching solution containing 50 mM lysine, 50 mM glycine, and 50 mM ammonium chloride, and permeated with 0.1% NaHCa buffer solution of Triton X-100 for 1 min. After 1 h of blocking with 1% BSA solution, HAECs were incubated with a primary antibody to caveolin-1 (200 times dilution with 0.1% BSA solution) for 1 h. The HAECs treated with anti-caveolin-1 IgG were incubated with 10 nm colloidal gold conjugated anti-rabbit IgG (10 times dilution with 0.1% BSA solution) for 1 h and treated with PBS containing 2.5% glutaraldehyde for 15 min. These fixed specimens of HAECs were postfixed with Osmium (0.1%) in 0.1 M PBS buffer. The cells were rinsed with PBS and distilled water, dehydrated with ethanol, and embedded in epoxy resin (EPON 812, TAAB Laboratories Equipment Ltd., UK) by polymerization for 72 h at 70 °C. Ultrathin sections of the embedded HAECs were cut at thickness of 70 nm with an ultramicrotome (Reichert-Nissei Ultracut N, Nissei Sangyo Co., Tokyo, Japan), mounted on electron microscope grids, stained with uranyl acetate/lead citrate, and then observed by TEM (Tecnai G2 *Sphera*, FEI, USA).

Specimens for the rapid-freeze, deep-etch, freeze-replica were prepared by the following method.[17] After a 1 h incubation with fluorescein-labeled nanoparticles (Flu-Am-PAPS), the HAECs were washed with the mammalian ringer solution (155 mM NaCl, 3 mM KCl, 2 mM $CaCl_2$, 1 mM $MgCl_2$, 3 mM NaH_2PO_4, and 5 mM HEPES brought to pH 7.4 with NaOH, plus 10 mM glucose). Immediately after being unroofed from the apical cell membrane, the basal cell membrane was fixed for 15 min in 1% paraformaldehyde/0.25% glutaraldehyde in buffer A (70 mM KCl, 5 mM $MgCl_2$, 3 mM EGTA, 30 mM HEPES buffer adjusted at pH 7.4 with KOH) and washed with the NaHCa buffer for 10 min three times. To identify the nanoparticles attached to the undercoat structure of plasma membrane, the detached basal side of plasma membrane of HAECs was labeled by treating with a primary antibody against the fluorescein molecule and a secondary antibody conjugated with 5 nm diameter colloidal gold. The labeled specimen was further fixed in 2% GA buffer on ice for 15 min. The specimen was washed in distilled water for 1 min before rapid freezing. The coverslip attached to the basal side of the HAECs was set on the plunger tip of the rapid freezing device (Polaron, U.S.A.) with the cytoplasmic surface of the plasma membrane down. The coverslip was fallen onto a polished pure copper block, which was precooled by liquid helium. The frozen coverslip was immersed in liquid nitrogen and was transferred into the freeze etching shadowing chamber (Bal-Tec BAF060, Liechtenstein). The cytoplasmic surface was deeply etched and rotary shadowed with platinum/carbon at an angle of 22° from the surface and with carbon from the top. The replica was removed from the coverslip in aqueous solution of 1% hydrofluoric acid. After the replica was washed with distilled water, the replica was mounted on mesh copper grid coated with polyvinyl Formvar (Nisshin EM, Japan). Finally, the sample grid was observed by TEM.

Nitric Oxide (NO) Detection. NO detection was carried out by referencing the previous literature.[18] HAECs were exposed to Dulbecco's modified Eagle medium (phenol red free DMEM, Invitrogen) containing 50 μM diaminorhodamine-4 acetoxymethyl ester (DAR-4 M AM; Daiichi pure chemicals) for 10 min. The DAR-4 M AM loaded sample was washed with DMEM (1 mL) and filled with 2 mL of DMEM for post incubation. Post incubation was performed for 15 min in a 37 °C, 5% CO_2 humidified incubator. The sample was rinsed with DMEM (1 mL) twice and filled with 1 mL of DMEM. Then, the dish was fixed on a microscope stage with adhesive tape. Fluorescence images were captured to monitor NO release by fluorescence microscope (IX-71 equipped with a temperature controlled stage (Microwarm Plate, Kitazato Supply) and a CCD camera (DP-70) Olympus) after the addition of DMEM (in case of resting state or after the cellular uptake of nanoparticles) or DMEM solution of bradykinin (1 μM) (in case of stimulation). Image capture was carried out every 30 s by initial 180 s of monitoring, then every 60 s by the end of monitoring at 900 s.

Western Blotting. HAECs cultured on a plastic culture dish (Iwaki, ϕ35 mm) were lysed with 40 μL of RIPA lysis buffer (Rockland, Gilbertsville, PA) for 5 min at 4 °C and scraped from the dish surface with a cell scraper. The lysates were collected and then centrifuged to remove insoluble materials at 10000*g* for 20 min. The supernatant was collected in a test tube. Protein concentration in the supernatant was determined by the Bio-Rad Protein Assay (Bio-Rad Laboratories, Hercules, CA) based on the method of Bradford. The supernatant was mixed with Laemmli sample buffer (Bio-Rad, Hercules, CA) containing 5% (V/V) β-mercaptoethanol and heated at 100 °C for 2 min. The reduced protein solutions, including 2 μg of the extracted proteins, were loaded into each well of 5−20% gradient SDS-PAGE gel (e-PAGEL, ATTO, Tokyo). The gel was run at 20 mA constant current in an electrophoresis chamber (AE6500, ATTO, Tokyo) plugged with a power supply (AE8135, ATTO, Tokyo). The proteins on a gel were transferred to a PVDF membrane (Clear Blot Membrane-P, ATTO, Tokyo) at 140 mA in a semi-dry electrophoretic transfer cell (AE6678, ATTO, Tokyo). The PVDF membrane was blocked with a blocking buffer (Blocking One-P, Nacalai Tesque, Kyoto) for 30 min at 20 °C and then incubated with a primary antibody (1000 times dilution with Can-Get-Signal; solution 1; Toyobo, Osaka) to each target protein (eNOS, phosphorylated eNOS at Ser1177, β-Tubulin) overnight at 4 °C. The target protein transferred on the PVDF membrane was reacted with horseradish peroxidase (HRP) conjugated secondary antibody (Cell Signaling, Danvers, Mass; 1000 times dilution with Can-Get-Signal (solution 2)) for 1 h at 20 °C and detected using colorimetric detection reagent (Ez West Blue, ATTO, Tokyo). The reagent contains 3,3′,5,5′-tetramethylbendidine (TMB), colorimetric reagent, and hydrogen peroxide, substrate for HRP. TMB yields blue color when oxidized with hydrogen peroxide (catalyzed by HRP). Blue bands indicating the target proteins appeared on a PVDF membrane after a PVDF membrane was treated with Ez West Blue. Colorimetric intensity of the bands on a PVDF membrane was measured by image capture using a digital scanner (GT-X700, EPSON, Tokyo) and image analysis software (Fluoview ver. 5.0; Olympus, Tokyo).

Results and Discussion

Polysiloxane Nanoparticles. In our previous report[15] we synthesized a novel amphiphilic polysiloxane and found that the amphiphilic polysiloxane formed nanoparticles with diameters of several tens of nanometers in water. In addition to the

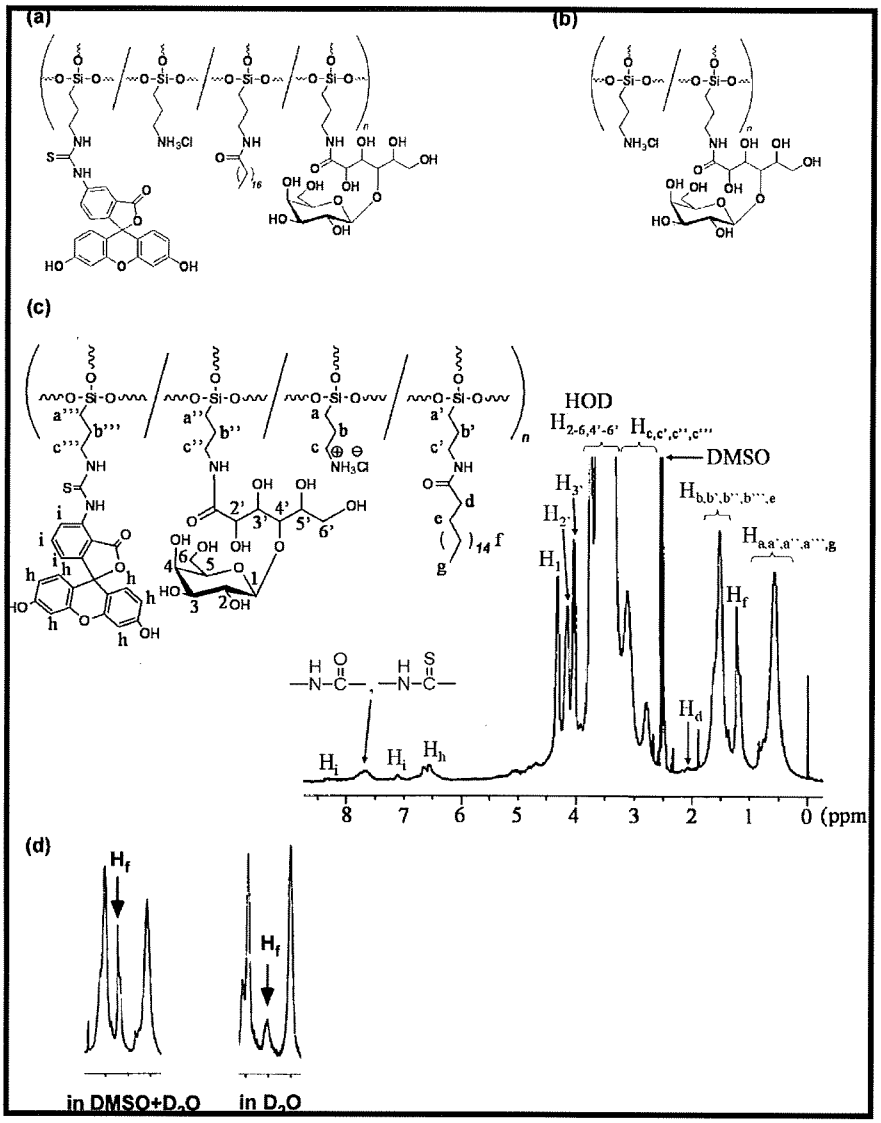

Figure 1. Chemical structure of (a) fluorescein-labeled amphiphilic polysiloxane (Flu-Am-PAPS) and (b) water-soluble sugar conjugated polysiloxane. (c) ^{1}H NMR spectrum of Flu-Am-PAPS in DMSO-d_6 (including a small amount of D_2O). Chemical shifts were referenced to DMSO (δ 2.5 ppm). (d) ^{1}H NMR signal of stearoyl group (H_f) observed in DMSO-d_6 (including a small amount of D_2O; left) and in D_2O (right).

amphiphilic polysiloxane, we obtained a fluorescence dye-labeled amphiphilic polysiloxane to track cellular uptake of the nanoparticles. We selected a fluorescein moiety as the fluorescent dye and synthesized the fluorescein-labeled amphiphilic polysiloxanes (Figure 1a) by using water-soluble poly(3-aminopropyl)siloxane (PAPS) having amino groups as a starting substrate as follows:[19] first, stearoyl groups as hydrophobic part and galactose moieties as hydrophilic part were introduced to PAPS in this order by the reactions of stearoyl chloride and lactobionolactone with the amino groups, respectively, giving an amphiphilic polysiloxane (Am-PAPS), and then, fluorescein-labeled polysiloxane (Flu-Am-PAPS: Figure 1a) was obtained by conjugation of fluorescein thioisocyanate to Am-PAPS. The molecular weight of PAPS as a polysiloxane backbone of Flu-Am-PAPS was measured by gel permeation chromatography with water as eluent and estimated to be 10300 g/mol (M_w/M_n = 1.41; pullulan was used as molecular weight standards). The substitution of amino groups in PAPS was estimated by ^{1}H NMR spectroscopy (Figure 1c) of the Flu-Am-PAPS; 2% of all amino groups was substituted for stearoyl group, 80% of those for galactose group, 4% of those for fluorescein and the rest of the amino groups were unreacted, that had been converted into the ammonium chlorides. For comparison, water-soluble sugar conjugated polysiloxane was synthesized (Figure 1b) by following the above method. The content of galactose moieties in the water-soluble polysiloxane was determined by ^{1}H NMR spectroscopy to be 43% (data not shown).

The amphiphilic polysiloxane (Am-PAPS/Flu-Am-PAPS) can form nanoparticles upon self-organization process in aqueous medium. Aqueous suspension of each amphiphilic polysiloxane was prepared by dispersing it (1 mg/mL) into cell culture medium for human aortic endothelial cells. The particle size of nanoparticles of the amphiphilic polysiloxane was measured by dynamic light scattering (DLS) measurement. The DLS measurement demonstrated that the Flu-Am-PAPS formed nanoparticles with a z-average diameter of 79 nm (0.290 for polydispersity index) in pure water. The particle size ranged from 40 to 400 nm (Figure 2a). About 48% of the nanoparticles comprised the group of nanoparticles whose diameter is less than 100 nm that is close to the caveolae size. The SEM image (Figure 2b) shows that the amphiphilic polysiloxane forms nanoparticles with diameters ranging from several tens of nanometers to 200 nm in diameter (average: 66 $\pm$ 30 nm). The difference in particle size bewteen DLS and SEM is attributable to the sample conditions (wet or dry) in these measurements.

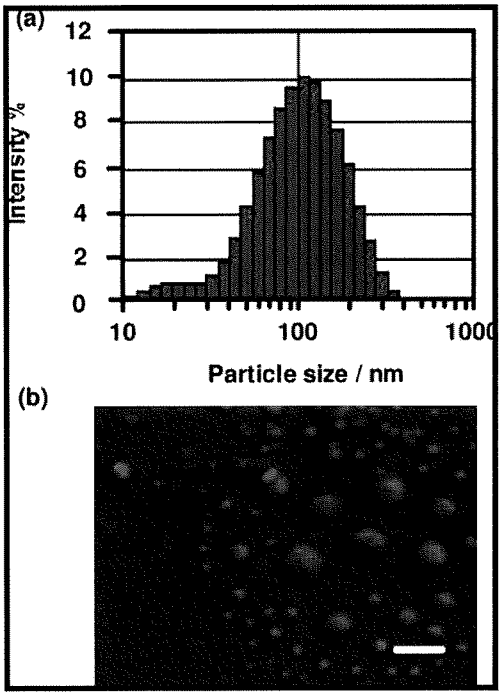

Figure 2. Particle size and morphology of nanoparticles of fluorescein-labeled amphiphilic polysiloxane (Flu-Am-PAPS). (a) Particle size histogram of nanoparticles of Flu-Am-PAPS. The nanoparticles were dispersed in pure water. (b) SEM image of Flu-Am-PAPS. Scale bar: 200 nm.

The nanoparticles had a slightly negative zeta potential (−0.9 mV) in the cell culture medium. The nanoparticle of Am-PAPS dispersed in phosphate buffered saline did not exhibit considerable change in particle size after one week storage at 37 °C (Figure S1a in Supporting Information). Furthermore, particle size measurement using DLS was carried out on the polysiloxane nanoparticles dispersed in cell culture medium containing 5% fetal bovine serum and found that one week storage of polysiloxane nanoparticles in serum containing culture medium at 37 °C caused little change in average particle size and particle size distribution (Figure S1b in Supporting Information). These data suggest that nanoparticles of Am-PAPS are stable in physiological condition. According to our recent report,[15] the NMR spectroscopy for the long alkyl side chains of the amphiphilic polysiloxane indicated that the signal intensity of protons in long alkyl chains become weak when the amphiphilic polysiloxane dissolved in D_2O was measured. Figure 1c shows that the signal observed around δ 1.25 ppm is ascribed to the protons of stearoyl chains attached to Flu-Am-PAPS and the signal intensity of the peak at δ 1.25 ppm of Flu-Am-PAPS dissolved in D_2O is weakened to the 76% of that of the peak at δ 1.25 ppm measured in DMSO (Figure 1d). The decrease in the intensity of the proton signal results from the restricted molecular motion of long alkyl chain and indicates that the molecular aggregation of Flu-Am-PAPS is driven by inter/intra hydrophobic association between stearoyl groups attached to the polysiloxane backbone.

Cellular Uptake of Nanoparticles by Human Aortic Endothelial Cells. Cellular uptake of the nanoparticles by HAECs was observed by fluorescence microscopy. HAECs were cultured for 72 h to obtain confluent culture of HAECs after cell suspension of HAECs was seeded on tissue culture dishes. At 72 h after cell seeding, cell culture medium was replaced with the polymer suspension of Flu-Am-PAPS. Then the HAECs were cultured in the polymer suspension for 15 min, 1, 3, 6, 24, 48, 72, and 144 h to monitor cellular uptake of the nanoparticles of Flu-Am-PAPS. The polymer suspension in cell culture dishes was exchanged daily during the incubation with Flu-Am-PAPS. Clearance of the incorporated nanoparticles from HAECs was observed after the nanoparticle suspension in culture dishes was replaced with EGM-2, growth medium for HAECs. For fluorescence microscopy observation, the cells were rinsed with 37 °C phosphate buffered saline (PBS), then were fixed by immersing into 10% formaldehyde neutral buffer solution at room temperature for 15 min and washed three times with PBS. Fluorescence images of the cells were taken by a fluorescence microscope equipped with a CCD camera at each incubation time. To evaluate cellular uptake of nanoparticles quantitatively, fluorescence intensity (F.I.) per image was determined by integrating the brightness at each pixel of fluorescence image using an image analysis software. The F.I. was normalized in a ratio of the F.I. at each incubation time over the F.I. at 6 h of incubation (the relative fluorescence intensity). The time course of the relative F.I. was plotted on the graph, Figure 3a (closed circles: uptake of nanoparticles; open circles: clearance of nanoparticles). HAECs incorporated progressively nanoparticles of Flu-Am-PAPS until 72 h of incubation and reached saturation thereafter until the end of observation at 144 h of incubation. Decline of F.I. after the removal of Flu-Am-PAPS from the cell culture dishes at 6 h of incubation indicates that the incorporated nanoparticles of Flu-Am-PAPS were gradually excreted from HAECs. However, 40% of the incorporated nanoparticles were still trapped in cytosol of HAECs at 138 h of post incubation (144 h of total incubation time). Meanwhile, the relative F.I. for the uptake dropped to only 2% of the control level (left bar in Figure 3b: 6 h at 37 °C) when HAECs were exposed to the nanoparticles at 4 °C of the incubation temperature for 6 h (middle bar in Figure 3b). Considerable cell detachment was not observed even after 6 h of the incubation at 4 °C. This means that cell culture of HAECs was maintained at a low culture temperature and the HAECs were alive. The temperature triggered dramatic decrease in the relative F.I. suggests that the nanoparticles are mainly incorporated into HAECs by endocytosis, not by adsorption to cell membrane. Endocytosis was restored after the HAECs exposed to low temperature environment were put back to the regular culture condition (cell culture at 37 °C). The reduced relative F.I. corresponding to the nanoparticle uptake at 4 °C increased to 90% of the relative F.I. that was measured after 6 h of incubation with Flu-Am-PAPS nanoparticles at 37 °C (left (incubation at 37 °C for 6 h) and right (incubation at 4 °C for 6 h and postincubation at 37 °C for 6 h) bars in Figure 3b). To ensure that the cellular uptake study was carried out under the condition that the dose of polysiloxane nanoparticles had little toxicity on HAECs, cytotoxicity of the polysiloxane nanoparticles in HAECs was evaluated by colorimetric cell viability assay using WST-8 as an indicator. Cell viability of HAECs was 95% when HAECs were cultured in the growth medium containing 1 mg/mL of Flu-Am-PAPS for 24 h. This suggests that the cellular uptake study was carried out under the condition that the polysiloxane nanoparticles did not exhibit cytotoxicity toward HAECs at 1 mg/mL of Flu-Am-PAPS.

Caveolae as Endocytic Pathway for Nanoparticles. Endocytosis is one of the important cell activities in internalization of various extracellular substances.[20] Endocytic pathways have been taken into account in targeted delivery of drug to vascular tissue. Caveolae are flask-shaped invaginations of cell membrane with diamters of 50−100 nm and are thought to function as

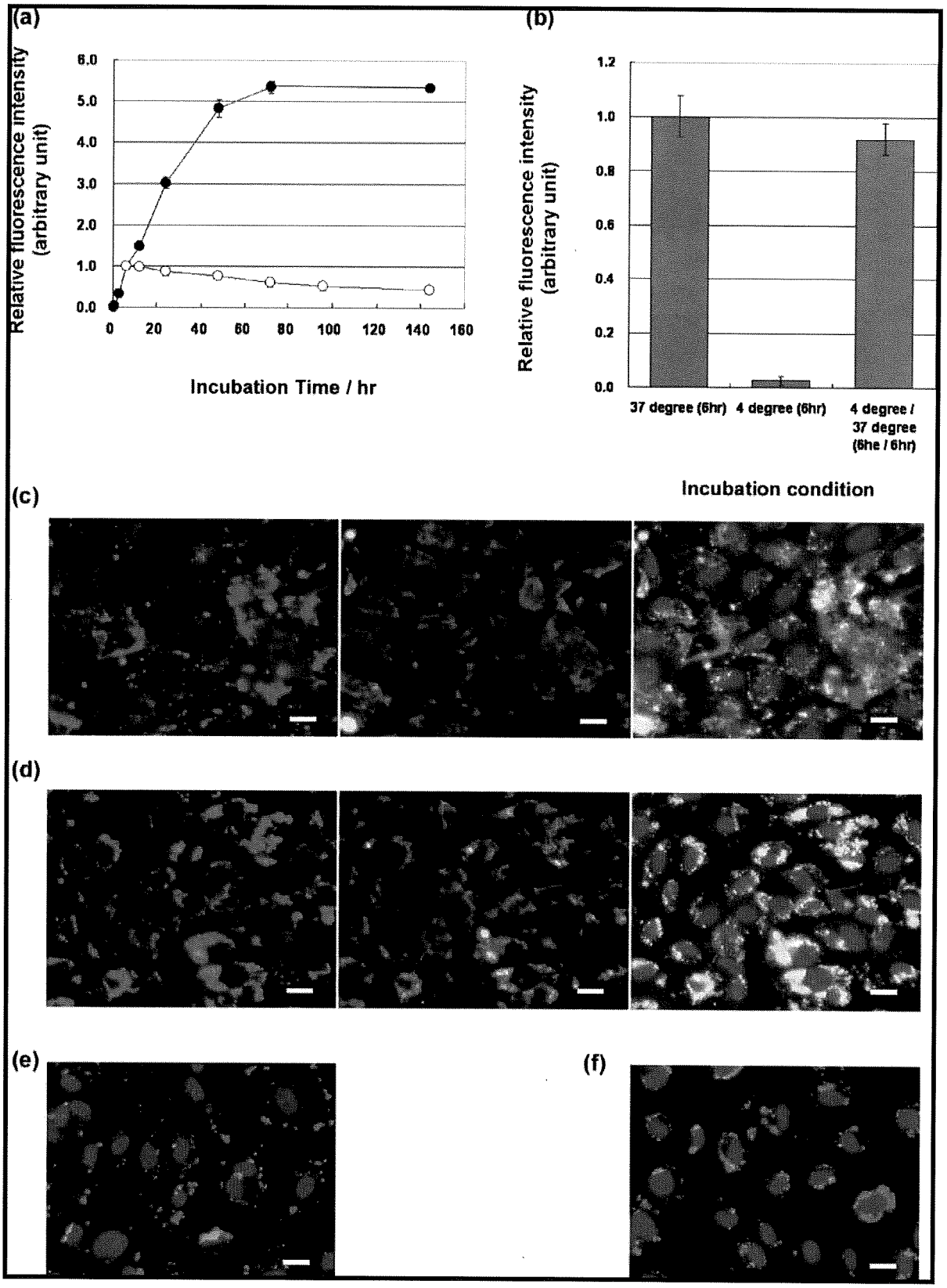

Figure 3. Cellular uptake of fluorescein-labeled amphiphilic polysiloxane (Flu-Am-PAPS). (a) Relative F.I. of Flu-Am-PAPS at each time of incubation with HAECs. The F.I. was measured by integrating brightness at each pixel of fluorescence image and normalized by F.I. at 6 h of incubation. Time course of the cellular uptake of Flu-Am-PAPS by HAECs was represented by closed circles (●). The clearance of the endocytosed Flu-Am-PAPS (○) from HAECs was monitored after HAECs were exposed to the nanoparticles of Flu-Am-PAPS for 6 h and incubated in growth medium. (b) Inhibition and recovery of cellular uptake of Flu-Am-PAPS followed by incubation temperature change (left, 6 h incubation at 37 °C; middle, 6 h incubation at 4 °C; and right, 6 h incubation at 4 °C and then 6 h incubation at 37 °C). Endocytic pathway in HAECs; localization of caveolin-1 and Flu-Am-PAPS in human aortic endothelial cells (HAECs). Caveolin-1 was detected by using primary antibody against caveolin-1 and TRITC-labeled secondary antibody against rabbit. Nucleuses of cells were stained with DAPI. Red: Caveolin-1. Green: Flu-Am-PAPS. Blue: nucleuses. (c) An image taken after 3 h incubation with Flu-Am-PAPS. (d) An image after 24 h incubation with Flu-Am-PAPS. Translocation and accumulation of the nanoparticles of Flu-Am-PAPS were confirmed in HAECs. (e) An image taken after 6 h incubation with Flu-Am-PAPS. (f) An image taken at 18 h of post incubation after the 6 h incubation with Flu-Am-PAPS. Nanoparticles of Flu-Am-PAPS accumulated around the cell nucleus. Scale bar: 20 μm.

platforms for endocytosis and signaling.[21] The caveolae-mediated pathway is prominent and ubiquitous endocytic mechanisms in vascular endothelial cells.[8] Figure 3c and d show fluorescence images of HAECs that incorporated fluorescein-labeled polysiloxane nanoparticles (green) and were immunostained for caveolin-1 (primary antibody against caveolin-1, TRITC-labeled secondary antibody against rabbit; red), which comprises the caveolae. Fluorescence image taken at 3 h of incubation time (Figure 3c) demonstrates that some of the green emissions from nanoparticles (left image in Figure 3c) are overlapped with red emissions from caveolin-1 (middle image in Figure 3c) to make yellow area (right image in Figure 3c). The yellow overlaps suggest that nanoparticles are localized at the caveolae. At 24 h of incubation time, nanoparticles (left image in Figure 3d) were localized as ring-like patterns of overlapped area around nucleuses of HAECs (right image in Figure 3d). This indicates that the nanoparticles of Flu-Am-PAPS were trapped into caveolae in plasma membrane and transported into cytosol of HAECs by 24 h of incubation. The peri-nuclear localization of the nanoparticles (Figure 3f) was also observed when HAECs were exposed to the nanoparticles for 6 h (Figure 3e) and incubated for 18 h after the medium containing nanoparticles was changed to growth medium containing no nanoparticles. The fluorescence imaging data indicate the following process for the uptake of the nanoparticles: (i) the nanoparticles are trapped at caveolae in plasma membrane, (ii) the nanoparticles are internalized into cytosol, and (iii) the nanoparticles are localized at peri-nuclear region. Furthermore, internalization of the nanoparticles into the cytosol of HAECs was confirmed by confocal laser scanning microscopy. The X-Y plane images of HAECs were taken as optical slices with 0.2 μm thick along *Z*-axis by confocal laser scanning microscope. Figure 4a shows fluorescence intensity profiles of Flu-Am-PAPS along the *Z*-direction in HAECs. The intensity profiles were obtained by integrating the brightness at each pixel over the whole area of each image, normalizing the intensity to the intensity at basal position ($Z = 0$ μm) and plotting the normalized intensity as a function of depth in a cell. The intenisty maximum was confirmed in each profile (arrow heads in the graph) and indicates the spatio and temporal position of the nanoparticles in HAECs. Although each profile has two maxima at $Z = 0$ μm and at other position in *Z*-axis respectively, the intensity maximum that we are discusing here is located above the basal level. The position of the intensity maximum shifted gradually from the apical side ($Z = 3$ μm) to the basal side ($Z = 0-1$ μm) of HAECs; $Z = 2.4-2.6$ μm at 1 h, $Z = 1.1-1.9$ μm at 3 h, $Z = 0.5-1.6$ μm at 6 h, and $Z = 0.4-1.2$ μm at 24 h. Thus, the peak shift clearly shows that the nanoparticles were trapped at the plasma membrane and internalized into the cytosol of HAECs.

The nanoparticles of the amphiphilic polysiloxane can fit into caveolae in the plasma membrane of HAECs, because the histogram of the particle size (Figure 2 (a)) for the nanoparticles of Flu-Am-PAPS indicates that at least 48% of the total population of the nanoparticles have diameters in the range of 10−100 nm, that is comparable to the dimension of caveolae (50−100 nm in both opening diameter and depth). Fluorescence microscope observation demonstrated the colocalization of the nanoparticles and caveolae (Figure 3c and d). To specify the endocytic pathway for the uptake of the nanoparticles we attempted to observe caveolae in HAECs by TEM. Specimens for TEM were prepared by the methods described in the materials and methods after HAECs were incubated with nanoparticles of gold nanoparticle labeled Am-PAPS (Au-Am-PAPS) or Flu-Am-PAPS at 37 °C for 3 h. The nanoparticles (Flu-Am-PAPS) uptaken by HAECs were detected by immunolabeling using anti-fluorescein IgG as a primary antibody and a secondary antibody attached to a gold nanoparticle (diameter: 5 nm). Here we observed TEM specimens by following the two different methods: conventional ultrathin section and rapid-freeze deep-etch immunoreplication.[22] The ultrathin section image (Figure 4b) shows that caveolae (round-shape structures with diameters of about 100 nm: indicated by a square in Figure 4b) are incorporated into cytosol and that dark dots (5−10 nm in diameter) of gold nanoparticles attached to polysiloxane are confirmed in the inner perimeter of caveolae vesicles (indicated by arrows in the inset of Figure 4b). Figure 4c shows the ultrathin section image of cytosol of the intact HAECs (not treated with the nanoparticles of Au-Am-PAPS), showing caveolae in cytosol of HAECs. Caveolae in cytosol of HAECs were detected by immunostaining of caveolin-1 using rabbit anti-caveolin-1 IgG and gold nanoparticles (10 nm of diameter) conjugated anti-rabbit IgG. Gold nanoparticles with 10 nm of diameter were specifically accumulated around the outer perimeter of round-shape structures with diameters of about 100 nm (Figure 4c). The result of immunodetection of caveolae indicates that the round shape structures in cytosol of HAECs are caveolae and provides an evidence that nanoparticles of Au-Am-PAPS are trapped in caveolae. Thus, the ultrathin section image of HAECs indicates that the nanoparticles of Au-Am-PAPS are trapped in caveolae at the plasma membrane of HAECs and are internalized into cytosol of HAECs. In addition to the nanoparticles trapped in caveolae, dark spots with a diameter of 5−10 nm (surrounded by circle in Figure 4b) were confirmed in cytosol of HAECs (Figure 4b). These spots are assigned to gold nanoparticles attached to amphiphilic polysiloxane (Au-Am-PAPS). The different localization of polysiloxane nanoparticles in cytosol of HAECs suggests that there are at least two different pathways in the cellular uptake of polysiloxane nanoparticles: caveolae and the other pathways, including clathrin-coated pits and macropinocytosis. Furthermore, we observed the undercoat structure on the cytoplasmic surface of the upper cell membrane using rapid-freeze deep-etch immunoreplication so as to obtain a detailed view of the cellular uptake of the nanoparticles via caveolae as main endocytic pathways for the uptake of polysiloxane nanoparticles. Fine structures of plasma membrane such as filamentous netlike structure of actin filaments, clathrin coated pits, and caveolae can be preserved by rapid freezing at the cooling speed of 10^5 °C/sec in specimen preparation. The extreme cooling speed does not cause any ice nucleation that can damage the organized structure of the membrane skeleton. In a recent study by Morone and Kusumi,[22] they applied the rapid-freeze replication method to the electron microscopy observation of the membrane skeleton and succeeded in viewing the fine structure of the membrane skeleton with nanometer scale resolution and demonstrating that the membrane skeleton mesh corresponds to the membrane compartment model that was suggested by the study of the diffusion of membrane molecules. Figure 4d and e are TEM images of the undercoat structure of the bottom cell membrane of HAECs before and after the exposure to the nanoparticles of Flu-Am-PAPS. The images were taken using a specimen that was processed by the rapid-freeze and deep-etch method. Caveolae (the characteristic striated round structures: 50−100 nm in diameter), clathrin-coated pits (the characteristic basket-like structures: 100−200 nm in diameter), and actin filaments were confirmed in the upper cell membrane of the intact HAECs (Figure 4d). The nanoparticles of Flu-Am-PAPS endocytosed

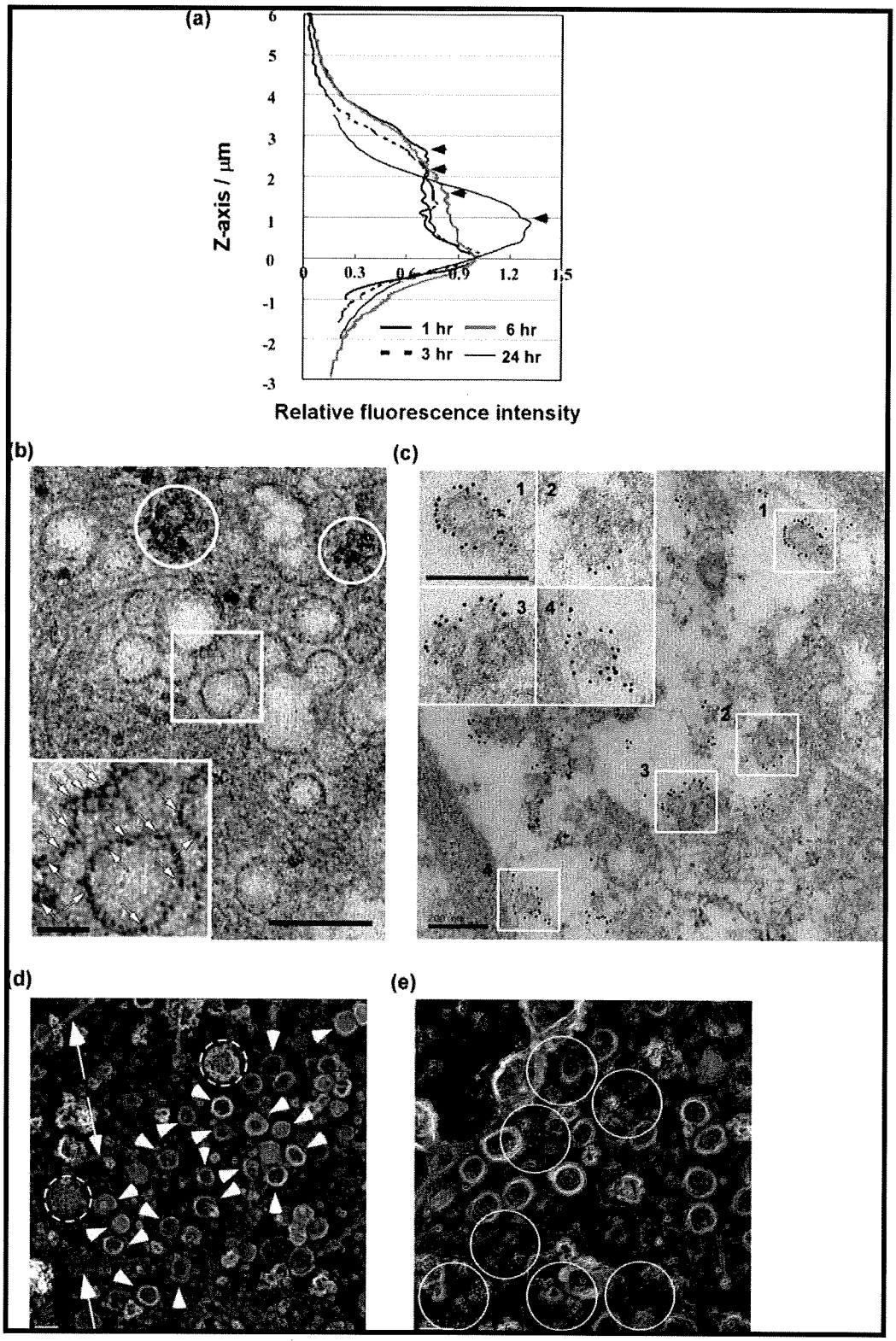

Figure 4. Internalization of nanoparticles of Flu-Am-PAPS in HAECs. (a) F.I. profiles of Flu-Am-PAPS in HAECs. F.I. was calculated by integrating brightness at each pixel over an optical section of confocal fluorescence image. The F.I. is plotted against the *Z*-axis position of each optical section in a confocal fluorescence image. Arrow heads indicates the intensity maximum in the profiles. The intensity maximum can reflect the most probable location of nanoparticles of Flu-Am-PAPS in HAECs at each incubation time. TEM observation of caveolae-mediated endocytosis in HAECs. Ultrathin sections were cut out from embedded HAECs in the direction parallel to the culture dish surface. In the ultrathin section image (b) the nanoparticles of Au-Am-PAPS were incorporated into cytosol of HAECs. Small black dots derived from gold nanoparticles attached to the amphiphilic polysiloxane with diameter of 5−10 nm are confirmed in the inner perimeter of caveolae (indicated by square). The inset is a two-times magnified image of the area indicated by square and shows clearly the small black dots in caveolae (indicated by arrows); (c) immunodetection of caveolae structures in cytosol of HAECs. Caveolae were confirmed by specific accumulation of 10 nm gold nanoparticles of secondary IgG (dark black dots) around the round structures with diameters of 100 nm in cytosol. Scale bars in Figure (b) and (c) represent 200 nm. Scale bars in the insets are 100 nm in (a) and 200 nm in (b). Rapid-freeze, deep-etch immunoreplication TEM images ((d) and (e)) show the undercoat structure of the upper cell membrane enriched in caveolae (indicated by arrow heads), (d), and the gold nanoparticles (white spots in circles) indicating the existence of the Flu-Am-PAPS in the caveolae-enriched area, (e). Other fine structures in (d) are clathrin coated pits (indicated by circle with broken line) and filamentous actin (indicated by arrow). Scale bar: 100 nm.

by HAECs were detected by indirect immunolabeling method with 5 nm diameter colloidal gold particles. Figure 4e shows that the gold particles for immunolabeling of Flu-Am-PAPS that were identified as the dispersed white spots in the TEM image appeared on the internal face of the upper cell membrane and that the gold particles were localized in the area where caveolae were densely accumulated (Figure 4e). The localization of gold particles in cell membrane means that the nanoparticles of Flu-Am-PAPS are localized in the caveolae accumulated area of the upper cell membrane and strongly suggests that caveolae can function as pathways in endocytosis when the nanoparticles of Flu-Am-PAPS are endocytosed into HAECs.

As for the particle size of the endocytosed nanoparticles, we extracted the endocytosed nanoparticles (Flu-Am-PAPS) from HAECs by using a surfactant free protein extraction method and measured the size of the extracted nanoparticles by DLS. According to the histogram of the particle size of the extracted nanoparticles in cytoplasmic fraction of HAECs (the histogram data are attached to Supporting Information as Figure S2), the histogram peak corresponding to the intact nanoparticles of Flu-Am-PAPS (the histogram peak at 150 nm in Figure S2b) shifted to smaller particle size (the histogram peak at 100 nm in Figure S2a) after the endocytosis into HAECs. This suggests that the nanoparticles of Flu-Am-PAPS comparable to the caveolae size are preferentially endocytosed by HAECs. Furthermore, we performed a DLS measurement of the collected sample including serum proteins of growth medium, nanoparticles of Flu-Am-PAPS, and cell debris after the incubation with HAECs and found that the histogram peak of the polysiloxane nanoparticles shifted from 150 nm (before incubation) to 250 nm (the histogram peak in Figure S2c) after the incubation with HAECs. This suggests that the polysiloxane nanoparticles that are larger than the caveolae size are more difficult to be endocytosed and remain after the incubation with HAECs. From the above experiment data of immunofluorescence microscopy, electron microscopy, and particle size measurement, it can be concluded that nanoparticles of amphiphilic polysiloxanes comparable to caveolae size are endocytosed via caveolae in plasma membrane of HAECs.

NO Release in HAECs. NO is a vasodilator synthesized in endothelial cells and plays important physiological roles such as the regulation of blood pressure and the inhibition of platelet adhesion.[7] As we mentioned the endocytic pathways for the uptake of the nanoparticles, caveolae are main routes in endocytosis and gateways to signal-transducing domain where inactive eNOS molecules are localized. It is an intriguing question whether the uptake of the nanoparticles can work in the activation of eNOS, if so, how it does. To study the influence of the nanoparticles on the expression of cell function, nitric oxide release of HAECs was monitored by using diaminorhodamine-4 acetoxymethyl ester (DAR-4 M AM), a fluorescent indicator for NO.[18] DAR-4 M AM can permeate through plasma membrane, be distributed to cytosol, specifically react with NO, and form a fluorescent triazole compound. HAECs were exposed to Dulbecco's modified Eagle medium containing 50 μM DAR-4 M AM for 10 min after the 6 h incubation with nanoparticles of Am-PAPS (0.1 mg/mL). NO release followed by the cellular uptake of polysiloxane nanoparticles could be detected by fluorescence microscope observation of the fluorescence intensity change that results from the triazole compound formation. Figure 5 shows the time profiles of fluorescence intensity of the reaction product derived from NO release after the incubation with nanoparticles (closed triangle), the treatment with bradykinin, endogenous eNOS activator (open circle), the incubation

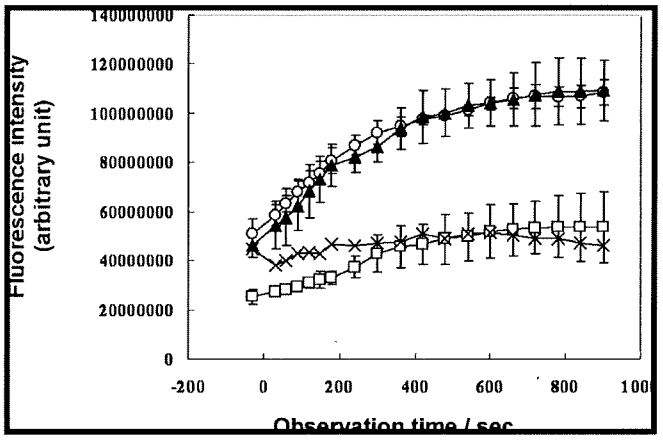

Figure 5. NO release in HAECs. Time profiles of NO release of HAECs. NO was detected by fluorescent indicator, diaminorhodamine-4 acetoxymethyl ester (DAR-4 M AM). The profile represented by open circles shows the NO release after the stimulation with bradykinin (n = 4). The profile represented by closed triangles shows the NO release after the cellular uptake of the nanoparticles of amphiphilic polysiloxane (n = 4). The profile represented by open squares shows the NO release after the cellular uptake of the sugar conjugated water-soluble polysiloxane (n = 3). The NO release profile in resting HAECs was indicated by cross (n = 3). The error bar in each data point is represented by standard deviation.

with water-soluble polysiloxane for positive control (open square), and the incubation in DMEM for negative control (cross symbol). After the uptake of nanoparticles, NO release of HAECs was enhanced up to the same release level that was observed when endothelial cells were stimulated by bradykinin. As a preliminary study about the effect of other nanomaterials on NO release in HAECs, we tested NO release level using commercially available polystyrene nanoparticles, micromer (Micromod, Rostock, Germany) in comparison with that using our polysiloxane nanoparticles. A similar trend in NO release was observed when HAECs were incubated with a growth medium containing 1 mg/mL of the polystyrene nanoparticles with 50 nm of diameter (time profile of NO release represented by open squares of Figure S3 in Supporting Information). However, the polystyrene nanoparticles with 200 nm of diameter did not enhance NO release level (time profile of NO release represented by closed squares of Figure S3 in Supporting Information). This suggests that nanoparticles with caveolae size could enhance NO release in HAECs. Furthermore, NO release followed by 6 h incubation with a nonassociative water-soluble sugar conjugated polysiloxane (Figure 1b; concentration, 1 mg/mL) was less than half of the NO release level induced by the amphiphilic polysiloxane nanoparticles and exhibited a time profile that was quite similar to that without stimulation (negative control: cross symbols in Figure 5). As a result of these data, the enhanced release of NO after the incubation with polysiloxane nanoparticles suggests that signal transduction leading to NO release is activated upon the cellular uptake of the nanoparticles via caveolae.

Activation of Endothelial Nitric Oxide Synthase (eNOS) Coupled to Nanoparticle Uptake. In resting endothelial cells, some of the eNOS molecules are inhibited by protein complex formation with caveolin-1, a constituent protein of caveolae. Cell stimulation with Ca^{2+}-mobilizing agonists such as bradykinin promotes calmodulin binding to eNOS and dissociation of eNOS from caveolin-1. The dissociated eNOS molecules can be detected in intracellular sites close to nucleus.[23] Such a subcellular migration of signaling proteins followed by their activation is known as translocation. The translocation of eNOS

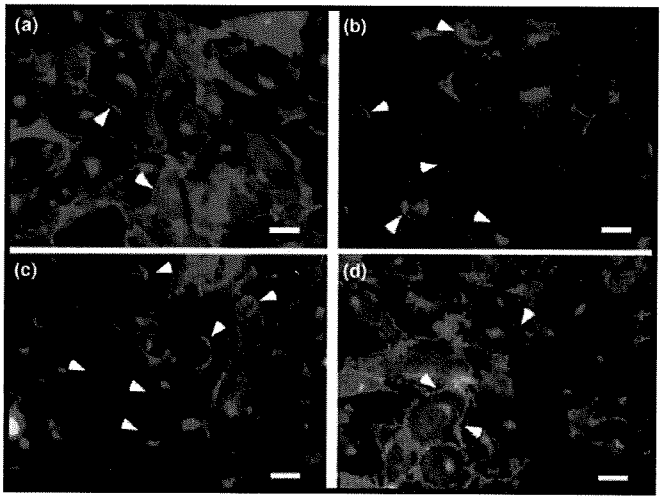

Figure 6. Translocation of eNOS in HAECs in response to bradykinin and upon cellular uptake of the nanoparticles of Am-PAPS. (a) Representative image of eNOS localization in resting HAECs (arrowhead). eNOS was redistributed from the cell periphery to intracellular sites near the nucleus (arrowheads in (b) and (c)) when HAECs were treated with 1 μM bradykinin for 5 min, (b), or were incubated with the nanoparticles of Am-PAPS (0.1 mg/mL) for 6 h, (c). eNOS did not translocate to peri-nuclear region of HAECs when HAECs were exposed to sugar conjugated water-soluble polysiloxane (1 mg/mL) for 6 h, (d). Scale bar in each image is 20 μm.

is followed by the activation of eNOS in endothelial cells.[23] Phosphorylation of eNOS on Ser^{1177} occurs concomitantly in the activation process of eNOS.[24] Here we studied the influence of nanoparticle uptake of HAECs on the eNOS activation with respect to the intracellular translocation and the phosphorylation of eNOS. Immunofluorescence imaging of HAECs using monoclonal antibody to eNOS demonstrated that eNOS bound to cell membrane (cell periphery: Figure 6a) translocate to the cell cytosol and the peri-nuclear region upon 5 min stimulation with 1 μM of bradykinin (Figure 6b). The translocation of eNOS was confirmed as ring-like patterns around nucleuses after the HAECs were exposed to nanoparticles of Am-PAPS for 6 h (Figure 6c). This suggests that caveolae-mediated endocytosis of nanoparticles in HAECs can be coupled to the eNOS activation and can work as an external stimuli in a signal transduction where membrane-bound eNOS are activated. Phosphorylation of eNOS at Ser^{1177} (P-eNOS) was detected by Western blot analysis. Figure 7a shows that phosphorylation of eNOS occurred when HAECs were incubated with the nanoparticles of Am-PAPS. The target proteins (eNOS and P-eNOS) transferred to PVDF membranes were detected by colorimetric reaction of TMB substrate. The protein levels of the target proteins were evaluated by measuring the intensity of the reaction product stained on the blotted bands. In Figure 7b the target protein levels were plotted against time of the incubation with nanoparticles. The total amount of eNOS gradually decreased to 65% of the initial amount of eNOS at 6 h of incubation while HAECs were incubated with polysiloxane nanoparticles (the time profile of eNOS: closed squares in Figure 7b). β-Tubulin, a loading control for Western blot analysis, exhibited a slight decrease in expression level during the incubation with polysiloxane nanoparticles (the time profile of β-tubulin: closed circles in Figure 7b), although the same amount of extracted proteins (2 μg) was applied to each lane in SDS-PAGE. This indicates that incubation with polysiloxane nanoparticles influences the expression level of eNOS in HAECs. On the other hand, the P-eNOS (Ser^{1177}) level gradually increased by 1.3 fold at 1 h of incubation and by 1.6-fold at

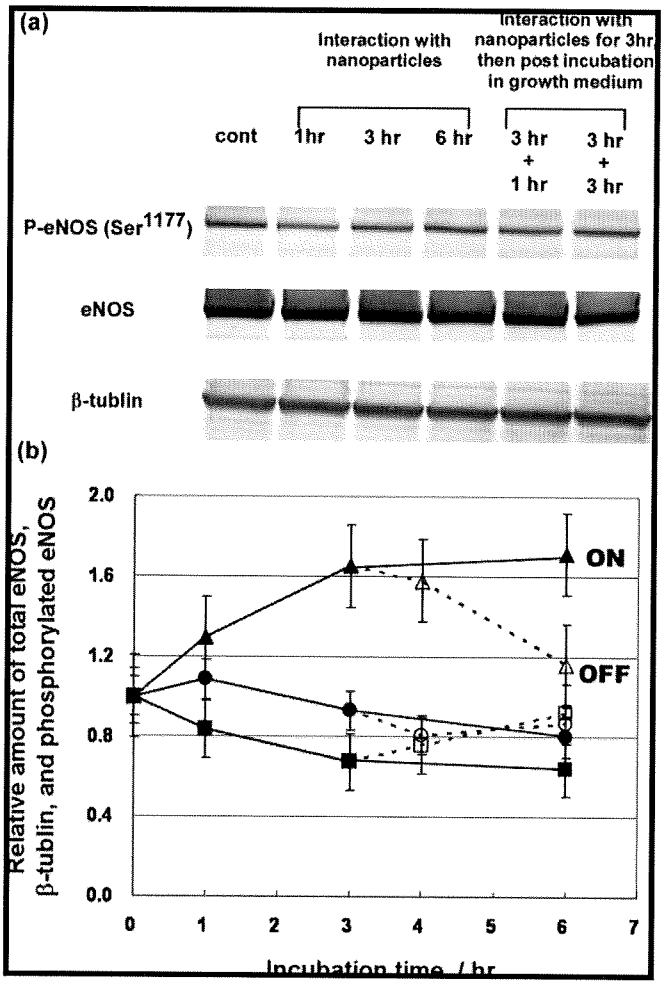

Figure 7. Nanoparticles of amphiphilic polysiloxane (Am-PAPS) stimulate phosphorylation of eNOS. HAECs were incubated with nanoparticles of Am-PAPS for the time period indicated. (a) Cell lysates were analyzed by Western blot with antibodies for phosphorylated eNOS-Ser1177, eNOS, and β-tubulin. (b) The bands of target proteins were quantified by measuring the colorimetric intensity. The graph shows the time course of the expression level of the target proteins (▲, △: P-eNOS, ■, □: e-NOS, and ●, ○: β-tubulin). The time courses represented by closed symbols demonstrate the expression level of the proteins of interest during the incubation with polysiloxane nanoparticles. The time course of the proteins of interest after the removal of polysiloxane nanoparticles at 3 h of incubation are depicted by open symbols and dotted lines. Each data point represents the means ± SE ($n = 3$).

3 h from the initial phosphorylation level of eNOS (the time profile of P-eNOS: closed triangles in Figure 7b). The expression level of P-eNOS reached saturation point at 6 h of incubation with polysiloxane nanoparticles. Thus, the activation of eNOS was followed by the cellular uptake of polysiloxane nanoparticles and the expression level of P-eNOS was maintained as long as HAECs were exposed to the nanoparticles. Furthermore, the expression levels of target proteins (eNOS, P-eNOS, and β-tubulin) were back to the initial level of each protein (time profiles (from 3 to 6 h of incubation time) indicated by open symbols and dotted lines in Figure 7b) when polysiloxane nanoparticles were removed from culture medium and HAECs were incubated in a fresh growth medium for 3 h after the removal of nanoparticles. These data suggest that phosphorylation of eNOS at Ser^{1177} is stimulated by interaction with nanoparticles and the enhanced level of phosphorylation is maintained transiently during the interaction with polysiloxane nanoparticles. Meanwhile, any eNOS translocation was not

observed at all when HAECs were exposed to the water-soluble sugar conjugated polysiloxane (concentration: 1 mg/mL) for 24 h (Figure 6d). According to the result of fluorescence image analysis for the estimation of the amount of the endocytosed polymers, the amount of the incorporated water-soluble polysiloxane at 24 h of the incubation was approximately 15% of that of the incorporated fluorescein-labeled nanoparticles (Flu-Am-PAPS) at 6 h of the incubation time (Figure S4 is available at Supporting Information). The water-soluble polysiloxane was certainly endocytosed by HAECs; however, the eNOS activation did not occur. These results suggest that the types of the polymers (nonassociative polymer chains or nanoparticles of amphiphilic polymers) exposed to cells and the pathways (caveolae or clathrin coated pits) selected in endocytosis are important factors that can influence the signal transduction in the regulation of cell function. Thus, we assume that the delivery of the nanoparticles targeted to caveolae facilitates eNOS activation (subcellular translocation and phosphorylation at Ser^{1177}) and the activated eNOS promotes NO release. The details of the mechanism underlying the eNOS activation upon the caveolae-mediated endocytosis of our polysiloxane nanoparticles is still under investigation and will be reported elsewhere.

Conclusion

In conclusion, the nanoparticles of amphiphilic polysiloxane were endocytosed via caveolae in human aortic endothelial cells and the uptake of the nanoparticles promoted nitric oxide release in HAECs. Caveolae is a membrane microdomain where various signal transduction molecules are accumulated and external stimuli are processed. Endothelial nitric oxide synthase is one of the constituent molecules in signal transduction and plays a significant role in regulation of vasorelaxation by synthesizing nitric oxide. Some of eNOS molecules are bound to caveolin-1 and deactivated in caveolae. Activation of eNOS is triggered in vivo by binding of physiological active molecules such as bradykinin, angiotensin-II, and estrogen to their corresponding receptors in endothelial cells. According to the recent study by Maniatis et al., eNOS-dependent NO production is coupled to caveolae-mediated endocytosis induced by albumin binding protein gp60 (albumin receptor).[25] In their case, NO release started just after gp60 activation by adding BSA and lasted up to 20 min. Phosphorylation of eNOS accompanied by gp60 activation was confirmed at just 30 s after the addition of BSA. This means that BSA uptake via caveolae in rat lung microvascular endothelial cells is quickly processed as an external signal and leads to NO release. In our study, a delay of 15−60 min between the beginning of the nanoparticle uptake and the onset of the induced phosphorylation of eNOS was observed. This kind of delay was rather observed in the phosphorylation of eNOS that was stimulated by shear stress to bovine aortic endothelial cells.[26] Sustained phosphorylation of eNOS is another feature of eNOS activation that is followed by nanoparticle uptake of HAECs. We found that the phosphorylation of eNOS lasted while HAECs were exposed to nanoparticles for 6 h. The phosphorylation of eNOS induced by gp60 activation lasted at most for 30 min. Furthermore, there was considerable difference in the working concentration of stimulants for the activation of eNOS between BSA (5 mg/mL) and our nanoparticles (0.1 mg/mL or less). We think that there are some different mechanisms in the activation of eNOS induced by caveolae-mediated endocytosis between former study using BSA and our current study using artificial nanoparticles. In any case, nanoparticle uptake by HAECs stimulates the activation of eNOS and raises the NO production. This means that nanoparticles can be regarded as extracellular signals. Concerning the influence of the interaction between nanomaterials with cells on the expression of cell function, a study on the behavior of bovine carotid arterial endothelial cells cultured on polyurethane nanocomposites demonstrated that cell migration could be regulated by the surface morphological change induced by blending gold nanoparticles with polyurethane and revealed that the promoted migration was associated with up-regulation of eNOS expression via the activation of PI3K/Akt signaling pathway.[27] The key phenomena explaining the promoted cell migration is signal transduction associated with the interaction between cells and the nanostructured surface and concomitant rearrangement of cytoskeleton. Meanwhile, our study deals with signal transduction associated with endocytosis of nanoparticles that are targeted to membrane microdomains of cells. As far as we know, this is the first demonstration that nitric oxide release in HAECs can be induced by the caveolae-mediated cellular uptake of artificial nano materials of synthetic polymer and that the uptake itself can work as external stimuli leading to the expression of a cell function. Thus, nanoparticle can work as an artificial signal substance whose signaling characteristics may be tuned by molecular design of constituting amphiphilic polymers as well as the nanoparticles can be used as nanocarriers in drug delivery system. In the drug delivery system the nanocarrier itself should be inert to targeted cells and tissues. However, as we demonstrated in this study, nanoparticles can influence cell functions; nanoparticles may not only promote the pharmacological effects of delivered drugs but also cause undesirable effects in the target tissues or cells. The molecular design of constituent molecules for nanoparticles and the interaction between nanoparticles and cells should be considered more carefully in terms of the activation of cell functions. Nevertheless, we expect that targeting delivery of nanoparticles including our polysiloxane nanoparticles to caveolae is a potential and novel medication to hypertension based on the regulation of NO release by switching of eNOS activation in a single cell.

Acknowledgment. T.N. thanks Professor Mitsuru Akashi and Dr. Takami Akagi of Osaka University for allocating instrument time of dynamic light scattering measurement, Dr. Tetsuji Yamaoka and Dr. Atsushi Mahara of National Cardiovascular Center Research Institute for allocating instrument time of fluorescence spectroscopy measurement, Dr. Tsutomu Furuzono of National Cardiovascular Center Research Institute for allocating instrument time of microplate reader in protein assay, and Mrs. Mina Kaneko for technical work in cell culture experiments. Part of this research was financially supported by Terumo Life Science Foundation in fiscal year of 2008.

Supporting Information Available. Supplementary data of nanoparticle size change in physiological condition, size of nanoparticles endocytosed, and cellular uptake of water-soluble polysiloxane. This material is available free of charge via the Internet at http://pubs.acs.org.

References and Notes

(1) Simons, K.; Ikonen, E. *Nature* **1997**, *387*, 569–572.
(2) Minshall, R. D.; Sessa, W. C.; Stan, R. V.; Anderson, R. G. W.; Malik, A. B. *Am. J. Physiol.* **2003**, *285*, L1179–L1183.
(3) Gratton, J.-P.; Bernatchez, P.; Sessa, W. C. *Circ. Res.* **2004**, *94*, 1408–1417.
(4) Wyatt, A. W.; Steinert, J. R.; Mann, G. E. *Biochem. Soc. Symp.* **2004**, *71*, 143–156.

(5) Vallance, P.; Chan, N. *Heart* **2001**, *85*, 342–350.
(6) McIntosh, D. P.; Tan, X.-Y.; Oh, P.; Schnitzer, J. E. *Proc. Natl. Acad. Sci. U.S.A.* **2002**, *99*, 1996–2001.
(7) Michel, T. *Braz. J. Med. Biol. Res.* **1999**, *32*, 1361–1366.
(8) Muro, S.; Koval, M.; Muzykantov, V. *Curr. Vasc. Pharmacol.* **2004**, *2*, 281–299.
(9) Sanvicens, N.; Marco, M. P. *Trends Biotechnol.* **2008**, *26*, 425–433.
(10) Conner, S.; Scmid, S. L. *Nature* **2003**, *422*, 37–44.
(11) Cruz, T.; Gaspar, R.; Donato, A.; Lopes, C. *Pharm. Res.* **1997**, *14*, 73–79.
(12) Mark, J. E.; Allcock, H. R.; West, R. In *Inorganic Polymers*, 2nd ed.; Oxford University Press: New York, 2005; pp 154−199.
(13) Kichler, A.; Sabourault, N.; Décor, R.; Leborgne, C.; Schmutz, M.; Valleix, A.; Danos, O.; Wagner, A.; Mioskowski, C. *J. Controlled Release* **2003**, *93*, 403–414.
(14) Moghimi, S. M.; Hunter, A. C.; Murray, J. C. *Pharmacol. Rev.* **2001**, *53*, 283–318.
(15) Beppu, K.; Kaneko, Y.; Kadokawa, J.; Mori, H.; Nishikawa, T. *Polym. J.* **2007**, *39*, 1065–1070.
(16) Tominaga, H.; Ishiyama, M.; Ohseto, F.; Sasamoto, K.; Hamamoto, T.; Suzuki, K.; Watanabe, M. *Anal. Commun.* **1999**, *36*, 47–50.
(17) Heuser, J. *Traffic* **2000**, *1*, 545–552.
(18) Kojima, H.; Hirotani, M.; Nakatsubo, N.; Kikuchi, K.; Urano, Y.; Higuchi, T.; Hirata, Y.; Nagano, T. *Anal. Chem.* **2001**, *73*, 1967–1973.
(19) Kaneko, Y.; Iyi, N.; Kurashima, K.; Matsumoto, T.; Fujita, T.; Kitamura, K. *Chem. Mater.* **2004**, *16*, 3417–3423.
(20) Durin, G.; Cottin, S.; Blanc, E.; Rees, A. R.; Temsamani, J. *J. Biol. Chem.* **2003**, *278*, 31192–31201.
(21) Drab, M.; Verkade, P.; Elger, M.; Kasper, M.; Lohn, M.; Lauterbach, B.; Menne, J.; Lindschau, C.; Mende, F.; Luft, F. C.; Schedl, A.; Haller, H.; Kurzchalia, T. V. *Science* **2001**, *293*, 2449–2452.
(22) Morone, N.; Fujiwara, T.; Murase, K.; Kasai, R.; Ike, H.; Yuasa, S.; Usukura, J.; Kusumi, A. *J. Cell Biol.* **2006**, *174*, 851–862.
(23) Prabhakar, P.; Thatte, H. S.; Goetz, R. M.; Cho, M. R.; Golan, D. E.; Michel, T. *J. Biol. Chem.* **1998**, *273*, 27383–27388.
(24) Fleming, I.; Busse, R. *Am. J. Physiol.* **2003**, *284*, R1–R12.
(25) Maniatis, N.; Brovkovych, V.; Allen, S. E.; John, T. A.; Shajahan, A. N.; Tiruppathi, C.; Vogel, S. M.; Skidgel, R. A.; Malik, A. B.; Minshall, R. D. *Circ. Res.* **2006**, *99*, 870–877.
(26) Boo, Y. C.; Sorescu, G.; Boyd, N.; Shiojima, I.; Walsh, K.; Du, J.; Jo, H. *J. Biol. Chem.* **2002**, *277*, 3388–3396.
(27) Hung, H. S.; Wu, C. C.; Chien, S.; Hsu, S. H. *Biomaterials* **2009**, *30*, 1502–1511.

BM900128X

RESEARCH ARTICLE

AMERICAN JOURNAL OF medical genetics PART B
Neuropsychiatric Genetics

Sexually Dimorphic Effect of the Val66Met Polymorphism of *BDNF* on Susceptibility to Alzheimer's Disease: New Data and Meta-Analysis

Noriko Fukumoto,[1] Takashi Fujii,[2] Onofre Combarros,[3] M. Ilyas Kamboh,[4] Shin-Jen Tsai,[5] Sachio Matsushita,[6] Benedetta Nacmias,[7] David E. Comings,[8] Humberto Arboleda,[9] Martin Ingelsson,[10] Bradley T. Hyman,[11] Hiroyasu Akatsu,[12] Andrew Grupe,[13] Agnes Lumi Nishimura,[14] Mayana Zatz,[14] Kari M. Mattila,[15,16] Juha Rinne,[17] Yu-ichi Goto,[18] Takashi Asada,[19] Shun Nakamura,[1] and Hiroshi Kunugi[2]*

[1]Department of Biochemistry and Cellular Biology, National Institute of Neuroscience, National Center of Neurology and Psychiatry, Kodaira, Tokyo, Japan

[2]Department of Mental Disorder Research, National Institute of Neuroscience, National Center of Neurology and Psychiatry, Kodaira, Tokyo, Japan

[3]Neurology Service, University Hospital 'Marqués de Valdecilla', Santander, Spain

[4]Department of Human Genetics, Graduate School of Public Health, University of Pittsburgh, Pittsburgh, Pennsylvania

[5]Department of Psychiatry, Taipei Veterans General Hospital, Taipei, Taiwan

[6]National Hospital Organization, Kurihama Alcoholism Center, Yokosuka, Kanagawa, Japan

[7]Department of Neurological and Psychiatric Sciences, Florence, Italy

[8]Department of Medical Genetics, City of Hope Medical Center (Emeritus), Carlsbad Science Foundation, Monrovia, California

[9]Neurosciences Research Group, Institute of Genetics, School of Medicine, National University of Colombia, Bogota, Colombia

[10]Department of Public Health/Molecular Geriatrics, Uppsala University, Uppsala, Sweden

[11]Harvard Medical School, Massachusetts General Hospital, Charlestown, Massachusetts

[12]Choju Medical Institute, Fukushimura Hospital, Toyohashi, Aichi, Japan

[13]CNS Research Celera Diagnostics, Alameda, California

[14]Biology Department, Human Genome Research Center, Institute of Biosciences, University of São Paulo-IBUSP, São Paulo, Brazil

[15]Medical School, University of Tampere, Tampere, Finland

[16]Centre for Laboratory Medicine, Tampere University Hospital, Tampere, Finland

[17]Turku PET Centre, University of Turku, Turku, Finland

[18]Department of Mental Retardation and Birth Defect Research, National Institute of Neuroscience, National Center of Neurology and Psychiatry, Kodaira, Tokyo, Japan

[19]Department of Psychiatry, Institute of Clinical Medicine, University of Tsukuba, Tsukuba, Ibaraki, Japan

Received 3 December 2008; Accepted 15 April 2009

How to Cite this Article:
Fukumoto N, Fujii T, Combarros O, Kamboh MI, Tsai S-J, Matsushita S, Nacmias B, Comings DE, Arboleda H, Ingelsson M, Hyman BT, Akatsu H, Grupe A, Nishimura AL, Zatz M, Mattila KM, Rinne J, Goto Y, Asada T, Nakamura S, Kunugi H. 2010. Sexually Dimorphic Effect of the Val66Met Polymorphism of *BDNF* on Susceptibility to Alzheimer's Disease: New Data and Meta-Analysis.
Am J Med Genet Part B 153B:235–242.

Additional Supporting Information may be found in the online version of this article.
Grant sponsor: Health and Labor Sciences Research Grants; Grant sponsor: National Institute of Biomedical Innovation (NIBIO); Grant sponsor: Japan Society for the Promotion of Science (JSPS).
Noriko Fukumoto and Takashi Fujii contributed equally to this work.
Anges Lumi Nishimura's present address is Institute of Psychiatry, King's College London, MRC Centre for Neurodegenerative Research, Academic Neurology (PO43), De Crespigny Park, Denmark Hill, London, UK.
*Correspondence to:
Hiroshi Kunugi, M.D., Ph.D., Department of Mental Disorder Research, National Institute of Neuroscience, National Center of Neurology and Psychiatry, Kodaira, Tokyo 187-8502, Japan. E-mail: hkunugi@ncnp.go.jp
Published online 5 June 2009 in Wiley InterScience (www.interscience.wiley.com)
DOI 10.1002/ajmg.b.30986

Conflicting results have been reported as to whether genetic variations (Val66Met and C270T) of the brain-derived neurotrophic factor gene (BDNF) confer susceptibility to Alzheimer's disease (AD). We genotyped these polymorphisms in a Japanese sample of 657 patients with AD and 525 controls, and obtained weak evidence of association for Val66Met ($P = 0.063$), but not for C270T. After stratification by sex, we found a significant allelic association between Val66Met and AD in women ($P = 0.017$), but not in men. To confirm these observations, we collected genotyping data for each sex from 16 research centers worldwide (4,711 patients and 4,537 controls in total). The meta-analysis revealed that there was a clear sex difference in the allelic association; the Met66 allele confers susceptibility to AD in women (odds ratio = 1.14, 95% CI 1.05–1.24, $P = 0.002$), but not in men. Our results provide evidence that the Met66 allele of BDNF has a sexually dimorphic effect on susceptibility to AD.

Key words: **Alzheimer's disease (AD); brain-derived neurotrophic factor (BDNF); meta-analysis; polymorphism; sex difference**

INTRODUCTION

Alzheimer's disease (AD) is a common neurodegenerative disease and is neuropathologically characterized by loss and atrophy of basal forebrain cholinergic neurons and the limbic structures [Mattson, 2004]. Mutations in several genes are known to cause familial AD, namely those encoding amyloid precursor protein [Goate et al., 1991], presenilin-1 [Sherrington et al., 1995], and presenilin-2 [Levy-Lahad et al., 1995]. The ε4 allele of the apolipoprotein E (*APOE*) gene confers susceptibility to familial and sporadic AD [Saunders et al., 1993]. However, AD is a genetically complex disorder and these genetic markers for AD cannot explain the overall genetic susceptibility. Thus, additional genes may be involved in the development of AD.

Since neurotrophins such as nerve growth factor (NGF), brain-derived neurotrophic factor (BDNF), and neurotrophin-3 (NT-3) promote the development, regeneration, survival, and maintenance of function of neurons [Reichardt, 2006], polymorphisms of the genes encoding these proteins may confer susceptibility to neurodegenerative diseases. Several lines of evidence have suggested that *BDNF*, in particular, is an important candidate gene for susceptibility to AD. Reduced *BDNF* mRNA levels were observed in postmortem hippocampi and temporal cortices of patients with AD [Connor et al., 1997], and lower protein levels of BDNF in the entorhinal cortex were reported in AD [Hock et al., 2000]. Immunohistochemical and Western blotting studies revealed a selective decline of the BDNF/TrkB neurotrophic signaling pathway in the frontal cortex and hippocampus in AD [Ferrer et al., 1999].

Based on these observations, a number of genetic association studies have been performed for two polymorphisms of *BDNF*, Val66Met, and C270T. The non-synonymous polymorphism, Val66Met, is a functional single-nucleotide polymorphism (SNP), G to A substitution at nucleotide 196, which results in the Val66-to-Met amino acid change in the 5′ pro-region of the human BDNF protein [Ventriglia et al., 2002]. Two studies reported that the Met66 allele was significantly associated with an increased risk of AD [Saarela et al., 2006; Tsai et al., 2006], while one study reported that the Val66 allele was the risk-increasing allele [Matsushita et al., 2005]. The majority of studies, however, have found no significant association (Supplementary Fig. 1) [Ventriglia et al., 2002; Bagnoli et al., 2004; Combarros et al., 2004; Nacmias et al., 2004; Bian et al., 2005; Bodner et al., 2005; Desai et al., 2005; Lee et al., 2005; Li et al., 2005; Nishimura et al., 2005; Vepsalainen et al., 2005; Akatsu et al., 2006; Forero et al., 2006; Zhang et al., 2006; He et al., 2007; Huang et al., 2007]. The C270T polymorphism in the non-coding region of *BDNF* was detected by our group and found to be associated with late-onset AD [Kunugi et al., 2001]. Subsequently, two other groups reported that the T270 allele was significantly associated with an increased risk of AD [Nishimura et al., 2004; Olin et al., 2005], while one group reported the opposite [Saarela et al., 2006]. Other studies reported no significant association (Supplementary Fig. 2) [Riemenschneider et al., 2002; Bagnoli et al., 2004; Nishimura et al., 2004; Bodner et al., 2005; Desai et al., 2005; Lee et al., 2005; Matsushita et al., 2005; Akatsu et al., 2006; Tsai et al., 2006; Zhang et al., 2006; Huang et al., 2007]. These conflicting results require further investigation.

METHODS

Case–Control Study Sample

We genotyped 657 patients with AD (427 females; 73.5 years [SD] 8.7) and 525 healthy controls (305 females; 67.1 years [SD] 10.3) who were recruited around the Tokyo Metropolitan area, Japan. Diagnoses were made by neurologists according to the National Institute of Neurological and Communicative Diseases and Stroke/Alzheimer's Disease and Related Disorders Association (NINCDS-ADRDA) criteria [McKhann et al., 1984] for "probable AD." The numbers of individuals with and without a family history of dementia were 211 and 425, respectively, while the remaining 21 individuals had undetermined family histories. Controls were interviewed and those who had a family history of dementia within their first-degree relatives were not enrolled in the study. All subjects were biologically unrelated Japanese individuals. After description of the study, written informed consent was obtained from every subject. The study protocol was approved from the ethics committee of the National Center of Neurology and Psychiatry, Japan.

Genotyping

The two SNPs of *BDNF* were genotyped using the TaqMan 5′-exonuclease allelic discrimination assay. TaqMan probes of the "Assay-On-Demand" (C__11592758_10) for Val66Met (rs6265) and TaqMan primers (forward: GGAGCCAGAATCGGAACCA; reverse: CCAGCGCTTGCCTACCT) and probes (VIC: CTCACGGGTCCCCG; FAM: CTCACGAGTCCCCG) of the "Assay-by-Design" for C270T and Universal PCR Master Mix were obtained from Applied Biosystems (Foster City, CA). Thermal cycling conditions for the polymerase chain reaction (PCR) were one cycle at 95°C for 10 min followed by 40 cycles of 95°C for 15 sec and 58°C for 1 min. After amplification, the allele-specific fluorescence was measured on ABI PRISM 7900 Sequence Detection

System (Applied Biosystems). Genotype data were read blind to the case–control status. We also genotyped the subjects for the *APOE* gene, according to the methods of Wenham et al. [1991].

Meta-Analysis

To examine whether there was a possible sex difference in the effect of these polymorphisms on AD in a larger sample, we organized a multi-center collaborative study and performed a meta-analysis. We searched for published case–control association studies of the Val66Met or C270T polymorphism with AD in the PubMed database (National Center for Biotechnology Information; NCBI; www.ncbi.nlm.nih.gov/), using combinations of terms "BDNF," "brain-derived neurotrophic factor," "polymorphism," "Val66Met," "C270T," "C-270T," and "Alzheimer." Additionally, reference lists of these and relevant articles, and the AlzGene Database (www.alzforum.org/) [Bertram et al., 2007] were referred to. As a result, 23 association studies of AD with Val66Met (Supplementary Table III) and 18 with C270T (Supplementary Table IV) were identified. Then an e-mail calling for participation in the collaborative study was sent to corresponding and first authors. Sixteen research groups for the Val66Met and 12 for the C270T responded and participated in this study. Genotype data with information on sex were combined.

Genotypes in the control groups from all research groups were in Hardy–Weinberg equilibrium. In the meta-analysis, heterogeneity, publication bias, sensitivity analysis, and Rosenthal's failsafe N were determined. Meta-analytic procedures were carried out using Comprehensive Meta-Analysis v.2.0 (Biostat, Inc., Englewood, NJ). To confirm that there was no significant difference in the allele distributions of patients and controls between the collected and the uncollected data (i.e., studies whose authors did not respond to us), Breslow–Day tests were performed using R software (R Development Core Team, 2007). With respect to Val66Met, the summary data for the Breslow–Day tests are shown in Supplementary Table V. There was no significant difference between the collected and uncollected data ($\chi^2 = 2.0$, df = 1, $P = 0.15$).

RESULTS

Case–Control Study

Genotype distributions for Val66Met, C270T, and *APOE* were in Hardy–Weinberg equilibrium for both patients and controls (data not shown). Genotype distributions for *APOE* were significantly different between the patients and controls as expected ($P = 2 \times 10^{-18}$) (Supplementary Table I). Genotype and allele distributions for Val66Met are shown in Table I. There was a trend towards an increased frequency of the Met66 allele in patients compared to controls ($P = 0.063$). When men and women were examined separately, the allele distribution differed between the two groups in females (odds ratio [OR] = 1.30, 95% CI = 1.05–1.60, $P = 0.017$), but not in males (OR = 1.02, 95% CI = 0.78–1.32, $P = 0.91$) (Table I).

The genotype and allele distributions for C270T are shown in Supplementary Table II. There was no significant difference in the genotype or allele distribution between the patients and controls.

TABLE I. Genotype and Allele Distributions for the Val66Met Polymorphism of BDNF in Patients With Alzheimer's Disease and Controls

	Genotype distribution								Allele distribution					
	Patients				Controls					Patients		Controls		
	n	Val/Val	Val/Met	Met/Met	n	Val/Val	Val/Met	Met/Met	*P*-value, df = 2	Val	Met	Val	Met	*P*-value, df=1
Total	657	218 (0.33)	319 (0.49)	120 (0.18)	525	197 (0.38)	249 (0.47)	79 (0.15)	0.18 ($\chi^2 = 3.4$)	755 (0.57)	559 (0.53)	643 (0.61)	407 (0.39)	0.063 ($\chi^2 = 3.5$)
Female	427	142 (0.33)	205 (0.48)	80 (0.19)	305	122 (0.40)	143 (0.47)	40 (0.13)	0.057 ($\chi^2 = 5.7$)	489 (0.57)	365 (0.60)	387 (0.63)	223 (0.37)	0.017 ($\chi^2 = 5.7$)
Male	230	76 (0.33)	114 (0.50)	40 (0.17)	220	75 (0.34)	106 (0.48)	39 (0.18)	0.96 ($\chi^2 = 0.09$)	266 (0.58)	194 (0.44)	256 (0.58)	184 (0.42)	0.91 ($\chi^2 = 0.01$)

TABLE II. Genotype and Allele Distributions for the Val66Met Polymorphism of *BDNF* in Female Subjects

		Genotype distribution								Allele distribution			
		Patients				Controls				Patients		Controls	
Study	Ethnicity	n	Val/Val	Val/Met	Met/Met	n	Val/Val	Val/Met	Met/Met	Val	Met	Val	Met
Akatsu et al. [2006]	Asian	58	16	36	6	86	30	42	14	68	48	102	70
Bian et al. [2005]	Asian	108	20	67	21	105	36	47	22	107	109	119	91
He et al. [2007]	Asian	318	92	152	74	332	97	170	65	336	300	364	300
Matsushita et al. [2005]	Asian	340	117	170	53	321	104	154	63	404	276	362	280
Tsai et al. [2006]	Asian	84	19	50	15	101	33	50	18	88	80	116	86
Current study	Asian	427	142	205	80	305	122	143	40	489	365	387	223
Subtotal		1,335	406	680	249	1,250	422	606	222	1,492	1,178	1,450	1,050
Combarros et al. [2004]	Caucasian	161	107	47	7	155	105	44	6	261	61	254	56
Desai et al. [2005]	Caucasian	669	449	201	19	411	287	115	9	1,099	239	689	133
Li et al. [2005] (UCSD)[a]	Caucasian	87	51	32	4	226	150	67	9	134	40	367	85
Li et al. [2005] (WashU)[b]	Caucasian	248	163	81	4	215	150	60	5	407	89	360	70
Li et al. [2005] (UK)[c]	Caucasian	265	178	73	14	270	192	73	5	429	101	457	83
Nacmias et al. [2004]	Caucasian	58	36	19	3	61	39	22	0	91	25	100	22
Saarela et al. [2006]	Caucasian	68	45	21	2	56	46	10	0	111	25	102	10
Subtotal		1,556	1,029	474	53	1,394	969	391	34	2,532	580	2,329	459
Desai et al. [2005]	African-American	46	42	4	0	33	31	2	0	88	4	64	2
Forero et al. [2006]	Mixed	73	51	20	2	115	90	23	2	122	24	203	27
Lee et al. [2005]	Unknown	61	31	28	2	38	20	14	4	90	32	54	22
Total		3,071	1,559	1,206	306	2,830	1,532	1,036	262	4,324	1,818	4,100	1,560

[a]UCSD sample from the University of California, San Diego.
[b]WashU sample from the Washington University.
[c]UK sample from Cardiff University, Wales College of Medicine and King's College London.

TABLE III. Genotype and Allele Distributions for the Val66Met Polymorphism of *BDNF* in Male Subjects

		Genotype distribution								Allele distribution			
		Patients				Controls				Patients		Contorls	
Study	Ethnicity	n	Val/Val	Val/Met	Met/Met	n	Val/Val	Val/Met	Met/Met	Val	Met	Val	Met
Akatsu et al. [2006]	Asian	37	9	22	6	22	5	11	6	40	34	21	23
Bian et al. [2005]	Asian	95	29	46	20	134	37	68	29	104	86	142	126
He et al. [2007]	Asian	195	63	93	39	243	68	115	60	219	171	251	235
Matsushita et al. [2005]	Asian	147	54	77	16	150	46	69	35	185	109	161	139
Tsai et al. [2006]	Asian	91	24	42	25	88	31	45	12	90	92	107	69
Current study	Asian	230	76	114	40	220	75	106	39	266	194	256	184
Subtotal		795	255	394	146	857	262	414	181	904	686	938	776
Combarros et al. [2004]	Caucasian	76	42	31	3	63	38	23	2	115	37	99	27
Desai et al. [2005]	Caucasian	329	216	98	15	260	169	82	9	530	128	420	100
Li et al. [2005] (UCSD)	Caucasian	94	54	38	2	126	81	39	6	146	42	201	51
Li et al. [2005] (WashU)	Caucasian	140	88	45	7	134	87	45	2	221	59	219	49
Li et al. [2005] (UK)	Caucasian	72	46	26	0	89	56	28	5	118	26	140	38
Nacmias et al. [2004]	Caucasian	25	12	10	3	36	16	16	4	34	16	48	24
Saarela et al. [2006]	Caucasian	29	16	13	0	45	35	7	3	45	13	77	13
Subtotal		765	474	261	30	753	482	240	31	1,209	321	1,204	302
Desai et al. [2005]	African-American	18	17	1	0	12	11	1	0	35	1	23	1
Forero et al. [2006]	Mixed	28	21	7	0	53	41	11	1	49	7	93	13
Lee et al. [2005]	Unknown	34	14	19	1	32	12	16	4	47	21	40	24
Total		1,640	781	682	177	1,707	808	682	217	2,244	1,036	2,298	1,116

Also when sexes were examined separately, no significant association was found for either sex.

Meta-Analysis

With respect to Val66Met, individual studies contained 64–998 patients with AD and 45–671 controls, and the combined sample consisted of 4,711 patients and 4,537 controls (Supplementary Table III). There was no heterogeneity across studies (total: $Q = 26.7$, $df = 21$, $P = 0.18$; men: $Q = 16.0$, $df = 15$, $P = 0.38$; women: $Q = 13.5$, $df = 15$, $P = 0.56$). Thus, we performed the fixed effects meta-analyses (Fig. 1, Tables II and III). The meta-analysis showed no significant association between AD and the Met66 allele (OR = 1.05, 95% CI = 0.98–1.11; $Z = 1.43$, $P = 0.15$; Supplementary Fig. 1). Meta-analysis of data in men and women separately revealed a significant association in women (OR = 1.14, 95% CI = 1.05–1.24; $Z = 3.05$, $P = 0.002$; Fig. 1A), but not in men (OR = 0.97, 95% CI = 0.87–1.08; $Z = -0.54$, $P = 0.59$; Fig. 1B). In the sensitivity analysis, the association of the Met66 allele with AD remained significant after removal of any one study (Supplementary Table VI): even if our data were removed, there remained a significant association for women (residual OR = 1.11,

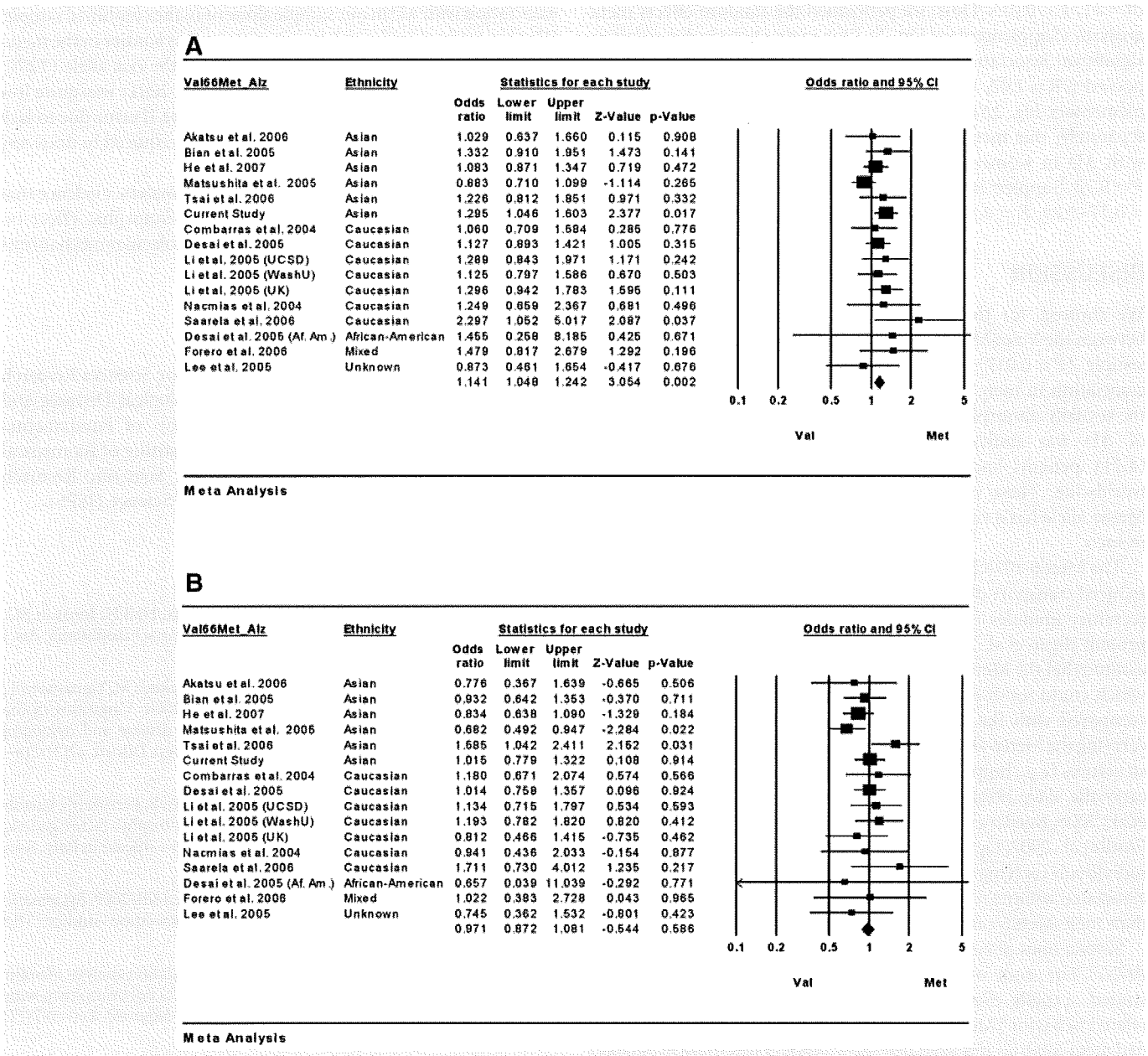

FIG. 1. Forest plots of meta-analysis on the possible association between the Val66Met polymorphism of *BDNF* and Alzheimer's disease in female (A) and male (B) subjects.

95% CI = 1.02–1.22; Z = 2.30, $P = 0.022$). The Rosenthal failsafe N for women was 31 studies. No evidence of publication bias was indicated by Egger's test (intercept = 0.80, 95% CI = −0.37 to 0.54, $t = 1.46$, $P = 0.17$).

Meta-analysis for the C270T polymorphism was performed in the same way. Eighteen studies were identified, of which 12, including ours, participated in the meta-analysis. The individual studies contained 58–722 AD cases and 42–525 controls, and the combined sample consisted of 2,963 subjects with AD and 2,756 controls (Supplementary Tables IV, VII, and VIII). There was a significant heterogeneity between studies (total: Q = 44.7, df = 17, $P < 0.01$; men: Q = 18.8, df = 11, $P = 0.065$; women: Q = 30.2, df = 11, $P < 0.01$). Thus, we performed the random effects meta-analyses (Supplementary Fig. 2). Our meta-analysis did not show significant association of AD with the T270 allele (random-effect pooled OR = 1.07, 95% CI = 0.83–1.39; Z = 0.54, $P = 0.59$; Supplementary Fig. 2A). Also when men and women were examined separately, our meta-analysis revealed no significant association with AD in women (OR = 1.08, 95% CI = 0.70–1.67; Z = 0.37, $P = 0.72$; Supplementary Fig. 2B) or in men (OR = 1.19, 95% CI = 0.77–1.84; Z = 0.78, $P = 0.43$; Supplementary Fig. 2C).

DISCUSSION

We showed, for the first time, a significant allelic association between the Val66Met of *BDNF* and AD in women in our Japanese sample ($P = 0.017$). In contrast, we did not observe such an association in men. When the multi-center study was organized, the sexually dimorphic effect of the Val66Met on the development of AD was similarly observed in the much larger sample (4,711 patients and 4,537 controls) from 16 research centers worldwide. These results provide evidence suggesting that the Met66 allele has a risk-increasing effect on AD in women, but not in men.

The Met66-BDNF protein has been shown to be associated with reduced transport of BDNF from the Golgi region to appropriate secretory granules in neurons, compared with the Val66-BDNF protein [Egan et al., 2003; del Toro et al., 2006]. It is reasonable to assume that the Met66 is associated with lower secretion of BDNF, which could result in attenuation of the survival signal of BDNF, compared with the Val66. In accordance with this, individuals carrying the Met66 allele have been reported to have decreased brain structures (e.g., hippocampus) than those individuals who did not carry the allele [Pezawas et al., 2004; Szeszko et al., 2005; Agartz et al., 2006; Bueller et al., 2006; Ho et al., 2006; Nemoto et al., 2006; Frodl et al., 2007; Liguori et al., 2007]. Of note, we found that female individuals carrying the Met66 allele showed more widespread age-associated volume reduction in the dorsolateral prefrontal cortices than male Met66 carriers [Nemoto et al., 2006].

Several lines of evidence suggest the sexual dimorphic effects of *BDNF*. The study of *BDNF* conditional knockout mice demonstrated sexually dimorphic effects in depression- and anxiety-related behavior [Monteggia et al., 2007]. A recent sexually stratified meta-analysis reported that the Val66Met was more important in the development of major depressive disorder in men than in women [Verhagen et al., 2008]. In Parkinson's disease as well, a sex difference in the effect of *BDNF* was reported [Foltynie et al., 2005]. Many epidemiological studies reported higher prevalence and incidence of AD in women than in men [Fratiglioni et al., 1997]. In an animal model of neurodegenerative diseases, aged female mice were more sensitive to kainic acid-induced excitotoxicity to neurons, compared with aged males [Zhang et al., 2008]. These findings are in line with our observations of the sexually dimorphic effect of *BDNF* on AD. Indeed, estrogen plays an important role in the expression of BDNF. Estrogen receptors co-localize with BDNF-synthesizing neurons in the forebrain [Miranda et al., 1993] and estrogen induces BDNF expression through the estrogen response element [Sohrabji et al., 1995].

With respect to the C270T, we obtained no evidence for an association with AD in our sample alone or in the combined sample. We observed a significant heterogeneity across studies in the meta-analysis. In addition, the allele frequency of the risk allele (T270) reported in the original study [Kunugi et al., 2001] was quite low (0.03 in total), indicating the possibility of type II error due to lack of statistical power. Thus, further studies are required to draw any conclusion.

In conclusion, we provided the first meta-analytic evidence that the Met66 allele of *BDNF* has a sexually dimorphic effect on susceptibility to AD. Studies elucidating the molecular mechanisms underlying this association are warranted.

ACKNOWLEDGMENTS

This study was supported by Health and Labor Sciences Research Grants (Research on Psychiatric and Neurological Diseases and Mental Health), the Program for Promotion of Fundamental Studies, in Health Sciences of the National Institute of Biomedical Innovation (NIBIO), and Grant-in-Aid for Scientific Research from the Japan Society for the Promotion of Science (JSPS).

REFERENCES

Agartz I, Sedvall GC, Terenius L, Kulle B, Frigessi A, Hall H, Jonsson EG. 2006. BDNF gene variants and brain morphology in schizophrenia. Am J Med Genet Part B 141B(5):513–523.

Akatsu H, Yamagata HD, Kawamata J, Kamino K, Takeda M, Yamamoto T, Miki T, Tooyama I, Shimohama S, Kosaka K. 2006. Variations in the BDNF gene in autopsy-confirmed Alzheimer's disease and dementia with Lewy bodies in Japan. Dement Geriatr Cogn Disord 22(3):216–222.

Bagnoli S, Nacmias B, Tedde A, Guarnieri BM, Cellini E, Petruzzi C, Bartoli A, Ortenzi L, Sorbi S. 2004. Brain-derived neurotrophic factor genetic variants are not susceptibility factors to Alzheimer's disease in Italy. Ann Neurol 55(3):447–448.

Bertram L, McQueen MB, Mullin K, Blacker D, Tanzi RE. 2007. Systematic meta-analyses of Alzheimer disease genetic association studies: The AlzGene database. Nat Genet 39(1):17–23.

Bian JT, Zhang JW, Zhang ZX, Zhao HL. 2005. Association analysis of brain-derived neurotrophic factor (BDNF) gene 196 A/G polymorphism with Alzheimer's disease (AD) in mainland Chinese. Neurosci Lett 387(1): 11–16.

Bodner SM, Berrettini W, van Deerlin V, Bennett DA, Wilson RS, Trojanowski JQ, Arnold SE. 2005. Genetic variation in the brain derived neurotrophic factor gene in Alzheimer's disease. Am J Med Genet Part B 134B(1):1–5.

Bueller JA, Aftab M, Sen S, Gomez-Hassan D, Burmeister M, Zubieta JK. 2006. BDNF Val66Met allele is associated with reduced hippocampal volume in healthy subjects. Biol Psychiatry 59(9):812–815.

Combarros O, Infante J, Llorca J, Berciano J. 2004. Polymorphism at codon 66 of the brain-derived neurotrophic factor gene is not associated with sporadic Alzheimer's disease. Dement Geriatr Cogn Disord 18(1):55–58.

Connor B, Young D, Yan Q, Faull RL, Synek B, Dragunow M. 1997. Brain-derived neurotrophic factor is reduced in Alzheimer's disease. Brain Res Mol Brain Res 49(1–2):71–81.

del Toro D, Canals JM, Gines S, Kojima M, Egea G, Alberch J. 2006. Mutant huntingtin impairs the post-Golgi trafficking of brain-derived neurotrophic factor but not its Val66Met polymorphism. J Neurosci 26(49): 12748–12757.

Desai P, Nebes R, DeKosky ST, Kamboh MI. 2005. Investigation of the effect of brain-derived neurotrophic factor (BDNF) polymorphisms on the risk of late-onset Alzheimer's disease (AD) and quantitative measures of AD progression. Neurosci Lett 379(3):229–234.

Egan MF, Kojima M, Callicott JH, Goldberg TE, Kolachana BS, Bertolino A, Zaitsev E, Gold B, Goldman D, Dean M, et al. 2003. The BDNF val66met polymorphism affects activity-dependent secretion of BDNF and human memory and hippocampal function. Cell 112(2):257–269.

Ferrer I, Marin C, Rey MJ, Ribalta T, Goutan E, Blanco R, Tolosa E, Marti E. 1999. BDNF and full-length and truncated TrkB expression in Alzheimer disease. Implications in therapeutic strategies. J Neuropathol Exp Neurol 58(7):729–739.

Foltynie T, Lewis SG, Goldberg TE, Blackwell AD, Kolachana BS, Weinberger DR, Robbins TW, Barker RA. 2005. The BDNF Val66Met polymorphism has a gender specific influence on planning ability in Parkinson's disease. J Neurol 252(7):833–838.

Forero DA, Benitez B, Arboleda G, Yunis JJ, Pardo R, Arboleda H. 2006. Analysis of functional polymorphisms in three synaptic plasticity-related genes (BDNF, COMT AND UCHL1) in Alzheimer's disease in Colombia. Neurosci Res 55(3):334–341.

Fratiglioni L, Viitanen M, von Strauss E, Tontodonati V, Herlitz A, Winblad B. 1997. Very old women at highest risk of dementia and Alzheimer's disease: Incidence data from the Kungsholmen Project, Stockholm. Neurology 48(1):132–138.

Frodl T, Schule C, Schmitt G, Born C, Baghai T, Zill P, Bottlender R, Rupprecht R, Bondy B, Reiser M, et al. 2007. Association of the brain-derived neurotrophic factor Val66Met polymorphism with reduced hippocampal volumes in major depression. Arch Gen Psychiatry 64(4):410–416.

Goate A, Chartier-Harlin MC, Mullan M, Brown J, Crawford F, Fidani L, Giuffra L, Haynes A, Irving N, James L, et al. 1991. Segregation of a missense mutation in the amyloid precursor protein gene with familial Alzheimer's disease. Nature 349(6311):704–706.

He XM, Zhang ZX, Zhang JW, Zhou YT, Tang MN, Wu CB, Hong Z. 2007. Lack of association between the BDNF gene Val66Met polymorphism and Alzheimer disease in a Chinese Han population. Neuropsychobiology 55(3–4):151–155.

Ho BC, Milev P, O'Leary DS, Librant A, Andreasen NC, Wassink TH. 2006. Cognitive and magnetic resonance imaging brain morphometric correlates of brain-derived neurotrophic factor Val66Met gene polymorphism in patients with schizophrenia and healthy volunteers. Arch Gen Psychiatry 63(7):731–740.

Hock C, Heese K, Hulette C, Rosenberg C, Otten U. 2000. Region-specific neurotrophin imbalances in Alzheimer disease: Decreased levels of brain-derived neurotrophic factor and increased levels of nerve growth factor in hippocampus and cortical areas. Arch Neurol 57(6):846–851.

Huang R, Huang J, Cathcart H, Smith S, Poduslo SE. 2007. Genetic variants in brain-derived neurotrophic factor associated with Alzheimer's disease. J Med Genet 44(2):e66.

Kunugi H, Ueki A, Otsuka M, Isse K, Hirasawa H, Kato N, Nabika T, Kobayashi S, Nanko S. 2001. A novel polymorphism of the brain-derived neurotrophic factor (BDNF) gene associated with late-onset Alzheimer's disease. Mol Psychiatry 6(1):83–86.

Lee J, Fukumoto H, Orne J, Klucken J, Raju S, Vanderburg CR, Irizarry MC, Hyman BT, Ingelsson M. 2005. Decreased levels of BDNF protein in Alzheimer temporal cortex are independent of BDNF polymorphisms. Exp Neurol 194(1):91–96.

Levy-Lahad E, Wasco W, Poorkaj P, Romano DM, Oshima J, Pettingell WH, Yu CE, Jondro PD, Schmidt SD, Wang K, et al. 1995. Candidate gene for the chromosome 1 familial Alzheimer's disease locus. Science 269(5226):973–977.

Li Y, Rowland C, Tacey K, Catanese J, Sninsky J, Hardy J, Powell J, Lovestone S, Morris JC, Thal L, et al. 2005. The BDNF Val66Met polymorphism is not associated with late onset Alzheimer's disease in three case-control samples. Mol Psychiatry 10(9):809–810.

Liguori M, Fera F, Gioia MC, Valentino P, Manna I, Condino F, Cerasa A, La Russa A, Clodomiro A, Paolillo A, et al. 2007. Investigating the role of brain-derived neurotrophic factor in relapsing-remitting multiple sclerosis. Genes Brain Behav 6(2):177–183.

Matsushita S, Arai H, Matsui T, Yuzuriha T, Urakami K, Masaki T, Higuchi S. 2005. Brain-derived neurotrophic factor gene polymorphisms and Alzheimer's disease. J Neural Transm 112(5):703–711.

Mattson MP. 2004. Pathways towards and away from Alzheimer's disease. Nature 430(7000):631–639.

McKhann G, Drachman D, Folstein M, Katzman R, Price D, Stadlan EM. 1984. Clinical diagnosis of Alzheimer's disease: Report of the NINCDS-ADRDA Work Group under the auspices of Department of Health and Human Services Task Force on Alzheimer's Disease. Neurology 34(7): 939–944.

Miranda RC, Sohrabji F, Toran-Allerand CD. 1993. Neuronal colocalization of mRNAs for neurotrophins and their receptors in the developing central nervous system suggests a potential for autocrine interactions. Proc Natl Acad Sci USA 90(14):6439–6443.

Monteggia LM, Luikart B, Barrot M, Theobold D, Malkovska I, Nef S, Parada LF, Nestler EJ. 2007. Brain-derived neurotrophic factor conditional knockouts show gender differences in depression-related behaviors. Biol Psychiatry 61(2):187–197.

Nacmias B, Piccini C, Bagnoli S, Tedde A, Cellini E, Bracco L, Sorbi S. 2004. Brain-derived neurotrophic factor, apolipoprotein E genetic variants and cognitive performance in Alzheimer's disease. Neurosci Lett 367(3): 379–383.

Nemoto K, Ohnishi T, Mori T, Moriguchi Y, Hashimoto R, Asada T, Kunugi H. 2006. The Val66Met polymorphism of the brain-derived neurotrophic factor gene affects age-related brain morphology. Neurosci Lett 397(1–2):25–29.

Nishimura AL, Oliveira JR, Mitne-Neto M, Guindalini C, Nitrini R, Bahia VS, de Brito-Marques PR, Otto PA, Zatz M. 2004. Lack of association between the brain-derived neurotrophin factor (C-270T) polymorphism and late-onset Alzheimer's disease (LOAD) in Brazilian patients. J Mol Neurosci 22(3):257–260.

Nishimura M, Kuno S, Kaji R, Kawakami H. 2005. Brain-derived neurotrophic factor gene polymorphisms in Japanese patients with sporadic Alzheimer's disease, Parkinson's disease, and multiple system atrophy. Mov Disord 20(8):1031–1033.

Olin D, MacMurray J, Comings DE. 2005. Risk of late-onset Alzheimer's disease associated with BDNF C270T polymorphism. Neurosci Lett 381(3):275–278.

Pezawas L, Verchinski BA, Mattay VS, Callicott JH, Kolachana BS, Straub RE, Egan MF, Meyer-Lindenberg A, Weinberger DR. 2004. The brain-derived neurotrophic factor val66met polymorphism and variation in human cortical morphology. J Neurosci 24(45):10099–11102.

Reichardt LF. 2006. Neurotrophin-regulated signalling pathways. Philos Trans R Soc Lond B Biol Sci 361(1473):1545–1564.

Riemenschneider M, Schwarz S, Wagenpfeil S, Diehl J, Muller U, Forstl H, Kurz A. 2002. A polymorphism of the brain-derived neurotrophic factor (BDNF) is associated with Alzheimer's disease in patients lacking the Apolipoprotein E epsilon4 allele. Mol Psychiatry 7(7):782–785.

Saarela MS, Lehtimaki T, Rinne JO, Huhtala H, Rontu R, Hervonen A, Roytta M, Ahonen JP, Mattila KM. 2006. No association between the brain-derived neurotrophic factor 196 G>A or 270 C>T polymorphisms and Alzheimer's or Parkinson's disease. Folia Neuropathol 44(1):12–16.

Saunders AM, Strittmatter WJ, Schmechel D, George-Hyslop PH, Pericak-Vance MA, Joo SH, Rosi BL, Gusella JF, Crapper-MacLachlan DR, Alberts MJ, et al. 1993. Association of apolipoprotein E allele epsilon 4 with late-onset familial and sporadic Alzheimer's disease. Neurology 43(8):1467–1472.

Sherrington R, Rogaev EI, Liang Y, Rogaeva EA, Levesque G, Ikeda M, Chi H, Lin C, Li G, Holman K, et al. 1995. Cloning of a gene bearing missense mutations in early-onset familial Alzheimer's disease. Nature 375(6534):754–760.

Sohrabji F, Miranda RC, Toran-Allerand CD. 1995. Identification of a putative estrogen response element in the gene encoding brain-derived neurotrophic factor. Proc Natl Acad Sci USA 92(24):11110–11114.

Szeszko PR, Lipsky R, Mentschel C, Robinson D, Gunduz-Bruce H, Sevy S, Ashtari M, Napolitano B, Bilder RM, Kane JM, et al. 2005. Brain-derived neurotrophic factor val66met polymorphism and volume of the hippocampal formation. Mol Psychiatry 10(7):631–636.

Tsai SJ, Hong CJ, Liu HC, Liu TY, Liou YJ. 2006. The brain-derived neurotrophic factor gene as a possible susceptibility candidate for Alzheimer's disease in a chinese population. Dement Geriatr Cogn Disord 21(3):139–143.

Ventriglia M, Bocchio Chiavetto L, Benussi L, Binetti G, Zanetti O, Riva MA, Gennarelli M. 2002. Association between the BDNF 196 A/G polymorphism and sporadic Alzheimer's disease. Mol Psychiatry 7(2):136–137.

Vepsalainen S, Castren E, Helisalmi S, Iivonen S, Mannermaa A, Lehtovirta M, Hanninen T, Soininen H, Hiltunen M. 2005. Genetic analysis of BDNF and TrkB gene polymorphisms in Alzheimer's disease. J Neurol 252(4):423–428.

Verhagen M, van der Meij A, van Deurzen PA, Janzing JG, Arias-Vasquez A, Buitelaar JK, Franke B. 2008. Meta-analysis of the BDNF Val66Met polymorphism in major depressive disorder: Effects of gender and ethnicity. Mol Psychiatry (in press).

Wenham PR, Price WH, Blandell G. 1991. Apolipoprotein E genotyping by one-stage PCR. Lancet 337(8750):1158–1159.

Zhang H, Ozbay F, Lappalainen J, Kranzler HR, van Dyck CH, Charney DS, Price LH, Southwick S, Yang BZ, Rasmussen A, et al. 2006. Brain derived neurotrophic factor (BDNF) gene variants and Alzheimer's disease, affective disorders, posttraumatic stress disorder, schizophrenia, and substance dependence. Am J Med Genet Part B 141B(4):387–393.

Zhang XM, Zhu SW, Duan RS, Mohammed AH, Winblad B, Zhu J. 2008. Gender differences in susceptibility to kainic acid-induced neurodegeneration in aged C57BL/6 mice. Neurotoxicology 29(3):406–412.

Experimental Neurology 221 (2010) 175–185

Contents lists available at ScienceDirect

Experimental Neurology

journal homepage: www.elsevier.com/locate/yexnr

Chronic stress-mutated presenilin 1 gene interaction perturbs neurogenesis and accelerates neurodegeneration

Shohko Kunimoto [a,*], Shun Nakamura [a,1], Keiji Wada [b], Takayoshi Inoue [a]

[a] Department of Biochemistry and Cellular Biology, National Institute of Neuroscience, National Center of Neurology and Psychiatry, Tokyo 187-8502, Japan
[b] Department of Degenerative Neurological Diseases, National Institute of Neuroscience, National Center of Neurology and Psychiatry, Tokyo 187-8502, Japan

ARTICLE INFO

Article history:
Received 30 July 2009
Revised 23 October 2009
Accepted 28 October 2009
Available online 4 November 2009

Keywords:
Neurodegenerative disease
Gene–environment interaction
Chronic intermittent restraint stress (CIRS)
Doublecortin (DCX)
Presenilin 1 (PS1)
Neurogenesis

ABSTRACT

Recent evidence suggests that supplemental factors coincident with aging and genetic determinants might be involved in the initial progression of Alzheimer's disease (AD). Early studies also indicate that chronic stress decreases hippocampal neurogenesis. Here, we investigate the effect of chronic stress on hippocampal neurogenesis using a transgenic mouse line (Tg) that overexpresses human presenilin 1 (PS1) with a familial AD (FAD)-related mutation in order to elucidate how the combination of chronic stress and mutated genes affects the cytoarchitecture in the hippocampal granule cell layer (GCL), which contributes to spatial learning and memory. Using an original chronic intermittent restraint stress (CIRS) protocol, we examined the effect of stress on hippocampal neurogenesis and neurodegeneration by immunohistochemical analysis. After short-term CIRS, neurodegeneration in Tg mice was significantly increased in the hippocampus with an earlier onset and progression than in the non-stressed Tg mice. Moreover, after long-term CIRS, transitional neurodegeneration appeared to proceed along the neuronal circuit involved in cognitive function in stressed Tg mice. Although the number of Pax6-positive (+) cells (mostly granule neuron precursors) did not significantly decrease during CIRS in both non-Tg and Tg mice, doublecortin (DCX) + neuronal progenitor cells in the GCL were markedly influenced in Tg mice; they were significantly reduced without stress compared with non-stressed non-Tg mice and significantly increased by CIRS compared with non-stressed Tg mice. We conclude from these results that diverse responses against stressful experiences among genetically predisposed individuals could lead to cognitive dysfunction through retardation of neuronal maturation and neurodegeneration.

Introduction

In human aging processes, frontal–striatal structural changes of the brain have been suggested to underlie mild memory difficulties. In Alzheimer's disease (AD) patients, cellular pathology characterized by amyloid plaques/neurofibrillary tangles (Golde et al., 2000; Mattson, 2004) results in progressive neurodegeneration and atrophy within medial temporal brain structures that associate with cognitive functions (Jack et al., 1992; Killiany et al., 1993); this leads directly to memory impairment via separate mechanisms (Buckner, 2004). At the molecular level, genetic mutations of presenilin 1 and 2 (PS1, PS2) or missense mutations in amyloid precursor protein increase amyloid β deposition, which are well investigated pathogenic traits of AD (Masters and Beyreuther, 1998). In addition, recent studies have highlighted the significance of adult neurogenesis in the hippocampal granule cell layer (GCL) for cognitive memory (Bruel-Jungerman et al., 2005; Drapeau et al., 2003; Gould et al., 1999; Imayoshi et al., 2008; Kempermann and Gage, 2002; Shors et al., 2001; Zhang et al., 2008), and an acceleration of neurogenesis has indeed been expected to provide therapeutic measures against cognitive impairment in AD (Kuhn et al., 2007; Ogita et al., 2005). In light of the progressive neurodegeneration seen in AD patients, even with increased generation of neuronal progenitor cells in the GCL (Jin et al., 2004), the elucidation of additional factors in granule cell regeneration is essential for clinical applications.

Several lines of evidence have thus far implied a correlation between the stress-induced decrease in hippocampal neurogenesis and deficits in the hippocampus-related memory (Gould and Tanapat, 1999; Nagata et al., 2009; Pardon and Rattray, 2008; Sandi, 2004;

Abbreviations: BrdU, 5-bromo-2′-deoxyuridine; AD, Alzheimer's disease; ANOVA, analysis of variance; CIRS, chronic intermittent restraint stress; CA3, Cornus Ammonis 3; DG, dentate gyrus; DCX, doublecortin; FAD, familial Alzheimer's disease; GCL, granule cell layer; NS, non-stressed control mice; PBS, phosphate buffered saline; PCtx, piriform cortex; +, positive; PS1, presenilin 1; RCtx, retrosplenial cortex; SEM, standard error of the mean; ST, stressed mice; SGZ, subgranular zone; L/V-Tg, transgenic mouse model of AD with overexpression of an FAD-type PS1; non-Tg, transgenic-negative mouse; W, week-old.

* Corresponding author. Present address: Department of Vascular Dementia Research, National Institute for Longevity Sciences, National Center for Geriatrics and Gerontology, 36-3 Gengo, Morioka-machi, Obu City, Aichi 474-8522, Japan. Fax: +81 562 46 8438.
E-mail address: kunimoto@nils.go.jp (S. Kunimoto).
[1] Present Address: Department of Biotechnology and Life Science, Tokyo University of Agriculture and Technology, 2-24-16 Naka-chou, Koganei-city, Tokyo 184-8588, Japan.

0014-4886/$ – see front matter © 2009 Elsevier Inc. All rights reserved.
doi:10.1016/j.expneurol.2009.10.020